Geophysical Journal International

Geophys. J. Int. (2014) **197,** 785–814
Advance Access publication 2014 February 21

doi: 10.1093/gji/ggu028

Global 3-D electromagnetic forward modelling: a benchmark study

Anna Kelbert,[1] Alexey Kuvshinov,[2] Jakub Velímský,[3] Takao Koyama,[4] Joseph Ribaudo,[5] Jin Sun,[1,2] Zdeněk Martinec[3] and Chester J. Weiss[6]

[1]*Department of Earth, Ocean, and Atmospheric Sciences, Oregon State University, Corvallis, OR, USA. E-mail: anya@coas.oregonstate.edu*
[2]*ETH Zurich, Switzerland*
[3]*Department of Geophysics, Faculty of Mathematics and Physics, Charles University in Prague, Czech Republic*
[4]*Earthquake Research Institute, University of Tokyo, Japan*
[5]*Scripps Institution of Oceanography, IGPP, La Jolla, CA, USA*
[6]*Department of Geosciences, Virginia Tech, Blacksburg, VA, USA*

Accepted 2014 January 22. Received 2014 January 22; in original form 2013 October 18

SUMMARY

Global electromagnetic (EM) induction studies have been the focus of increasing attention during the past few years. A primary stimulus for this interest has been increased quality, coverage and variety of the newly available data sets especially from recent low-Earth-orbiting satellite missions. The combination of traditional ground-based data with satellite-borne measurements presents intriguing opportunity to attack the most challenging problem of deep EM studies: the recovery of 3-D variations of electrical conductivity in the Earth's mantle. But the reliable inference of deep-Earth electrical properties depends on the accuracy and efficiency of the underlying forward modelling solutions used to model 3-D electromagnetic induction in a heterogeneous sphere. Several 3-D forward solvers have been proposed over the last decade, which are based on staggered-grid finite difference, integral equation, finite element and spherical harmonic-finite element approaches. However, there has been no systematic intercomparison amongst the solvers. The goal of this paper is to conduct such a study in order to explore the relative merits of the different approaches when confronted with a set of synthetic models designed to probe the numerical accuracy of each. The results of the intercomparison are presented along with performance metrics to help assess the computational costs associated with each solution.

Key words: Numerical solutions; Numerical approximations and analysis; Non-linear electromagnetics; Geomagnetic induction; Composition of the mantle.

1 INTRODUCTION

Numerical modelling of geophysical problems has experienced a rapid boom in recent decades, fuelled by unprecedented increase of computational resources, availability of new extensive data sets, as well as new developments in theoretical concepts, algorithms and programming languages and tools. The introduction of new methods and codes goes hand in hand with their mutual comparison, benchmarking and testing. The geophysical communities have been recently undertaking such activities in a wide spectrum of problems, such as glacial isostatic adjustement (Spada *et al*. 2011), mantle convection (Zhong *et al*. 2008), seismic tomography (Qin *et al*. 2008), geodynamo simulations (Christensen *et al*. 2001) and forward and inverse magnetotellurics (Miensopust *et al*. 2013). In this work, we study the performance of seven different approaches to the forward problem of global electromagnetic induction in spherical domain in various model scenarios.

Accurate numerical modelling of Maxwell's equations in a heterogenous spherical Earth is a critical milestone towards interpretation of ground-based and satellite magnetic field measurements. At the core of geoelectromagnetic inversion, a numerical solution to Maxwell's equations in the 3-D setting allows us to constrain the variations of electrical conductivity of the Earth's mantle. This physical parameter of the Earth is highly sensitive to melts and volatiles (e.g. Karato 1990; Yoshino *et al*. 2009; Karato 2011), and therefore provides us with a valuable additional constraint on the Earth's structure.

Unfortunately, the inverse problem of geoelectromagnetic induction is ill-posed, and the uncertainties in the electrical conductivity models are very hard to constrain. The ill-posedness of the problem is further amplified by sparsity of the available data sets, poor constraints on the external sources, and the numerical errors caused by the discrete computation of Earth's electromagnetic fields. Here, we focus on the issue of numerical errors, which are introduced at

various points in the numerical modelling procedure through factors such as model discretization, simplifying assumptions on the physics, and truncation. We address the problem of numerical inaccuracy by taking advantage of the range of numerical methods and modelling codes (Martinec 1999; Uyeshima & Schultz 2000; Velímský & Martinec 2005; Koyama *et al*. 2006; Kuvshinov 2008; Ribaudo *et al*. 2012; Sun & Egbert 2012) that have emerged in the last decade or two for a thorough cross-validation, and show that a systematic benchmarking exercise is valuable in constraining modelling errors which are otherwise very hard to pinpoint.

Besides the above mentioned modelling codes, we are aware of several other approaches that are not included in the present benchmark, either due to limited availability of their respective authors, or due to unresolved issues in the codes. Starting with the frequency-domain approaches, Everett & Schultz (1996) and Yoshimura & Oshiman (2002) implemented finite-element (FE) solvers based respectively on Lagrangian nodal, and Nédélec edge elements. Tarits & Mandéa (2010) used spherical-harmonic decomposition, and Runge–Kutta integration of the set of ordinary differential equations in the radial coordinate. Weiss (2010) used unstructured triangular finite-difference scheme that avoids spatial aliasing of the warped Cartesian grid and the topological significance of the pole nodes. Finally, Hamano (2002) introduced the first time-domain approach based on combination of spherical harmonics and 1-D finitexbrk differences.

We use Section 2 to introduce the numerical methods used in this benchmark. We proceed to design a suite of simple synthetic models for intercomparison of the existing numerical modelling codes for global geoelectromagnetic induction. Throughout this exercise, we focus on a set of numerically challenging model configurations that are easy to visualize, while also providing enough breadth to showcase the strong sides of each of the algorithms.

In a general 3-D environment, Maxwell's equations cannot be solved analytically and demand a numerical approach. The few semi-analytic solutions that exist are applicable to very specific 3-D model configurations: a heterogeneous infinitely thin layer (see Kuvshinov *et al*. 1999, and references therein) and eccentrically nested spheres (Everett & Schultz 1995; Martinec 1998). We have designed our benchmark models 1, 2and 3to correspond to simple, high contrast examples of these configurations. Sections 3 and 4 provide an intercomparison of a range of numerical approaches for computing the electromagnetic fields at the surface for a thin sheet of two variably conducting hemispheres: respectively, north/south (NS; model 1) and west/east (model 2). A nested sphere example is explored in Section 5. Section 6 contains a rectangular block model 4, in which a large conducting block is embedded in an otherwise layered Earth. The nested block model is intended to provide a counterpart to a nested sphere, however in this case sharp edges also need to be modelled, presenting an additional difficulty for approaches based in spectral model representation. On the other hand, models discussed in Section 7 are ideally suited to spectral modelling: this is a suite of three spherical harmonic models of variable degrees and orders. While providing a checkpoint similar to a checkerboard commonly used in seismic resolution testing, this set of models also serves as an example of smoothly varying electrical conductivity perturbation. Finally, Section 8 addresses the more intricate example of 3-D realistic surface conductance map overlaying a layered Earth. This is a variant on a thin sheet model that provides the complex pattern of conductivity contrasts expected to be found in the Earth's crust. Resolution, convergence criteria, and other settings of individual codes for each model are summarized in Section 9. The final Section 10 summarizes our findings and provides a comprehensive discussion of the strengths and drawbacks of each of the methods that have been analysed.

To simplify analysis and presentation, we have confined the modelling discussed in this paper to the more traditional P_1^0 source approximation, which has been historically applied to long period global EM studies. A suite of recent publications have challenged the use of this approximation at periods of ≈20 d and below (Fujii & Schultz 2002; Kelbert *et al*. 2009; Semenov & Kuvshinov 2012): the spatial structure of ionospheric sources, particularly at auroral latitudes, has a major effect on geomagnetic data. However, we have chosen to keep the source complexity issue outside of the scope of this benchmark intercomparison.

Traditionally, global electromagnetic induction had been performed using *C*-responses: scaled ratios of magnetic field components. These ratios cancelled the magnitude of the source, thus simplifying the analysis, however they also drastically reduced the amount of available data. In today's fully 3-D computational world, global EM tends to drift away from these historic simplifications. Therefore, in this intercomparison exercise we choose to work with full magnetic fields directly. To allow for this, the amplitude of the P_1^0 source is chosen in such a way that radial component of the external magnetic field at the North pole is equal to 100 nT. The four periods employed for this benchmark comparison are 6 hr, 1 d, 4 d and 16 d. The results are for the surface of the Earth (magnetic field components in nT). Time dependence is $\exp(i\omega t)$.

2 SUMMARY OF SOLUTION METHODS

Numerical methods employed in this study have been previously validated and published in a suite of independent publications. For the sake of self-sufficiency, we introduce these methods here, and refer an interested reader to the relevant publications for additional details.

For ease of presentation, the numerical codes we evaluate in this text, and the corresponding abbreviations are summarized in Table 1. Note that with the exception of Velímský & Martinec

Table 1. List of numerical codes for global geoelectromagnetic induction modelling that are evaluated in this paper.

Abbrev.	References	Method
KEL	Uyeshima & Schultz (2000); Kelbert *et al*. (2008)	3D staggered-grid finite differences
KOY	Koyama *et al*. (2006)	3D integral equations
KUV	Kuvshinov (2008)	3D integral equations
MAR	Martinec (1999)	3D spherical harmonic-finite elements
RIB	Ribaudo *et al*. (2012)	3D finite elements
SUN	Sun & Egbert (2012)	1D + surface thin-sheet integral equations
VEL	Velímský & Martinec (2005)	3D spherical harmonic-finite elements in the time domain

(2005, VEL), which is a time-domain solver, and Ribaudo *et al*. (2012, RIB), which has frequency and time domain capabilities, all other codes are implemented in the frequency domain. The methods fall, broadly, into four distinct categories: finite differences (KEL); finite elements (RIB); spherical harmonic-finite elements (MAR; VEL) and integral equations (KOY; KUV; SUN). Here, we discuss these general methods in just enough detail for the reader to follow the specifics of the model setup details discussed later.

2.1 Finite differences (FD)

Staggered-grid finite difference method was first implemented for the global EM induction problem by Uyeshima & Schultz (2000), following the Cartesian formulation of Mackie *et al*. (1994). This solves the vector Helmholtz equation for the magnetic field **H**, assuming harmonic time dependence of the form $e^{i\omega t}$,

$$\nabla \times (\rho \nabla \times \mathbf{H}) + i\omega\mu_0 \mathbf{H} = 0 \tag{1}$$

in a computational domain that includes the resistive air and conductive Earth's oceans, crust and mantle. Upper and lower boundary conditions are specified at the top of the air domain and at the CMB, respectively. Here, **H** denotes the magnetic field, ρ is the electrical resistivity (in Ω m), ω is frequency and μ_0 is the vacuum magnetic permeability. The code uses a stabilized bi-conjugate gradient method, and a divergence correction procedure is periodically applied to eliminate spurious solutions. The numerical code of Uyeshima & Schultz (2000) was carefully validated against a buried shell model (Kuvshinov *et al*. 1999) and the semi-analytic nested spheres solution of Martinec (1998; see also Sections 3 and 5 of this paper). Since then, the code has been modified in several substantial ways. The first (and critical) modification was made to allow for an arbitrary RHS, thus extending the solution to internal sources. This allowed a linearized global EM inversion to be performed (Kelbert *et al*. 2008, 2009). Further, yet unpublished, modifications include implementation of a secondary field formulation based on an analytic solution for a layered Earth similar to Sun & Egbert (2012). Specifically, for any perturbation $\delta\rho$ in the Earth's electrical resistivity structure, the full 3-D equation may be written as

$$\nabla \times (\rho + \delta\rho)(\nabla \times \delta\mathbf{H}) + i\omega\mu_0 \delta\mathbf{H} = -\nabla \times \delta\rho(\nabla \times \mathbf{H}). \tag{2}$$

We define the primary field as the solution of the analytic 1-D problem, and ρ as the corresponding layered resistivity structure. The 3-D deviations from this layered structure define $\delta\rho$. To compute the total magnetic field, we first solve for the primary field **H** and compute the RHS forcing for (2). We then run the generalized forward solver with the full 3-D electrical resistivity structure to compute the secondary magnetic fields $\delta\mathbf{H}$; $\mathbf{H} + \delta\mathbf{H}$ is the total magnetic field in the computational domain.

This method of solution is independent of the approximation employed in the original code that the magnetic field decay to zero at the CMB, and should therefore provide a somewhat more accurate solution method, while also allowing us to consider a smaller model domain that does not extend very deep into the lower mantle. It also allows to naturally extend the forward solution to an arbitrary external source model without further modifications to the core of the forward solver: indeed, only the primary (1-D) field is affected by the external source structure and merely provides a forcing for the perturbed (3-D) system. Throughout the exercises outlined in this paper, we have found that the differences in accuracy and computations costs for the two methods—brute-force forward modelling (FWD) and secondary field formulation (SFF)—are mostly not significant enough to warrant presentation. Any significant differences between the solutions are discussed explicitly.

Finally, the modified forward code (denoted by KEL throughout this manuscript) has been included into the modular system for electromagnetic induction (ModEM; Egbert & Kelbert 2012) and is now available to use with a suite of parallelized inverse solvers. These developments are viewed as a step towards joint inversion for conductivity and external sources. Discussion of these inversion strategies, however, is beyond the scope of this paper and will be presented elsewhere.

The method of staggered-grid finite differences is a structured grid numerical approach that is typically considered one of the most straightforward in implementation. As an added bonus, the discrete approximation to Maxwell's equations on a finite difference grid can always be written in a symmetric form (e.g. Egbert & Kelbert 2012) and convergence is easily achieved. The drawbacks of this structured, non-local approach include grid inflexibility: resolution cannot be easily increased locally in a region of high model contrasts without affecting the rest of the grid and significantly increasing computational expenses. It is also important to note that in global spherical coordinates, the North and South poles represent singularities in the structured grid and require special care. In this setup, major inaccuracies are introduced at the poles and propagate all the way to mid-latitudes if the convergence criteria are relaxed.

2.2 Finite elements (FE)

In this study, a FE solution for global EM induction (RIB) has been implemented with a commercially available, general-purpose FE method software program called FlexPDE. It allows the user to design and implement detailed simulations with a scripting language, leaving the mechanics of the solution of the partial differential equations to be managed by the program.

The use of a general purpose, commercial, FE package presents its own advantages and disadvantages. The primary advantage is ease of use—it is possible to quickly produce and run a fairly complex model via a short script, bypassing the time-consuming development and testing of source code. Such a model can be easily modified to create variations in both the model and the governing equations.

The convenience of general-purpose modelling software is balanced by its lack of optimization for a given problem. For example, the governing equations must be specified in a way that respects the constraints of the scripting language. In the case of global geomagnetic induction, this means that the magnetic vector potential must be used everywhere in the model, including in non-conductive regions where it would be more economical to substitute the magnetic scalar potential. Such a substitution would reduce the number of variables, allowing for a faster and likely more accurate solution, with less computational expense. Another example is modelling surface currents in the oceans and continents. These can be included in the model with creative use of boundary conditions at the Earth–space interface, but those boundary conditions must be specified in terms of the value of the electric or magnetic potentials, or in terms of the outward normal flux of those variables. This constraint can make it difficult to model electrical currents that have a radial component at the boundary between the mantle and the oceans.

In the frequency domain, the modelled induction equations are supplied in terms of the complex vector magnetic and scalar electric potentials, in a secondary field formulation. Models with thin shell

surface conductances include another solution variable, the complex scalar current function, that provides a boundary condition for the magnetic field at the Earth-space interface. The modelling domain includes the Earth's crust, mantle, and conductive core, as well as 10 Earth radii of resistive vacuum, which allows the secondary potentials to attenuate to zero at the model boundary.

Although there is nothing that prohibits an FE code from being used as the core compute engine for inversion, the FlexPDE package used here does not allow for low-level integration of forward and inverse computation. Nonetheless, an array of unique capabilities of this package make it potentially extremely valuable for forward modelling experiments. Advantages of FlexPDE compared to most other numerical approaches we discuss include the use of adaptive mesh refinement, time-domain capability, relative simplicity of coding and great flexibility in modelling, especially the ability to incorporate Earth rotation in the simulations within an arbitrary primary field structure.

This development has been particularly motivated by the need to re-evaluate the traditional external source approximations. The solution of Ribaudo *et al*. (2012) allows to directly consider Earth's rotation and the motions of satellites in time domain and thus to investigate the effects of source complexities on both the ground observatory and satellite data.

Like the finite difference solutions discussed earlier, the RIB code has also been independently validated for a range of special cases in Ribaudo *et al*. (2012).

2.3 Spherical harmonic-finite element method (SHFE)

The SHFE approach to the problem of EM induction in a sphere has been developed by Martinec (1999, MAR) in the frequency domain, and later implemented by Velímský & Martinec (2005, VEL) in the time domain. This approach offers two basic advantages over local methods. First, expanding the solution into spherical harmonics greatly simplifies the solution for a reduced complexity case of 1-D, depth-dependent conductivity. The problem is then decoupled into ordinary differential equations in the radial coordinate, and depending on the spherical harmonic degree j. Although this property is lost in the general 3-D case, where all spherical modes are coupled, the fast 1-D solution provides a natural pre-conditioner for iterative solution of the full problem in the frequency domain (Martinec 1999), or allows for an implementation of a semi-implicit scheme in the time-domain integration (Velímský & Martinec 2005). Secondly, the solution in the conductive Earth, even in the 3-D case, is easily coupled to the analytical solution for scalar magnetic potential in the surrounding insulating atmosphere.

In the frequency-domain approach (Martinec 1999), the spatial resolution of the solver is governed by the truncation degree of spherical harmonics, $j_{\max}$, and number of radial layers, $k_{\max}$. The finite-dimensional solution space is spanned by orthogonal, complex, vector spherical harmonic functions of colatitude and longitude, combined with 1-D, piecewise linear FEs in radial direction. The solenoidality of magnetic field is constrained by Lagrange multipliers, and the linear system is solved iteratively using preconditioned biconjugate gradient method. The iterative scheme avoids storage of the full system matrix. Only its left- or right-hand products with vectors are required, and these in turn contain coupling integrals of products of spherical harmonics and conductivity. For efficient evaluation fast Fourier transform in longitude, and Gauss–Legendre quadrature formula in colatitude are employed (Martinec 1989).

The choice of spherical harmonic basis is responsible also for the two main disadvantages of the method. The lateral resolution cannot be increased locally. Sharp lateral discontinuities in conductivity cannot be accurately approximated by polynomials, and will therefore lead to ringing artifacts that cannot be mitigated by simple increase of lateral resolution.

The original version of the method (Martinec 1999) used mathematically correct, but rather cumbersome boundary condition specifying the toroidal electrical field at the Earth's surface, which in turn can be derived from observations of the vertical magnetic field. The modified code presented in this benchmark incorporates the more traditional external magnetic field condition: the Gaussian coefficients of external magnetic field, either dipolar or with more complicated spatial structure are prescribed, and all magnetic field components are predicted at arbitrary position at the surface.

The time-domain variant of the SHFE method (Velímský & Martinec 2005, VEL) aims at the exploitation of low-orbit satellite measurements. Separation of spatial and temporal variations in data recorded along the vehicle's track represents an additional challenge that is mitigated by solving the EM induction by time-domain integration. The spatial discretization based on combination of vector spherical harmonics, and 1-D FEs is very similar to the one used in the frequency domain. The time integration uses a semi-implicit scheme: the dominant term based on radially varying average conductivity model is treated implicitly for stability, while the effect of lateral conductivity variations is evaluated using the known solution from the previous time step. This avoids the need to store a large system matrix, and again allows to use an efficient matrix-vector multiplication based on the fast Fourier transform and Gauss–Legendre formula. In addition to the spherical harmonic truncation degree $j_{\max}$, and number of radial layers $k_{\max}$, the choice of the time step Δt also influences the numerical accuracy of the solution.

In order to treat the benchmark examples excited by time-harmonic signals with period T (angular frequency $\omega = 2\pi/T$), the integration is started from zero initial magnetic field everywhere in the Earth, and excited by external field with $\sin(\omega t)$ time dependence. This avoids large transient signal at the start of the integration, but implies an additional phase shift of $\pi/2$ in the Fourier transform of the results. The system is evolved for at least 10 periods, and the spectral signals are obtained by simple integration over the last period,

$$\hat{\mathbf{B}}(\omega) = e^{\frac{\mathrm{i}\pi}{2}} \frac{1}{T} \int_{9T}^{10T} \mathbf{B}(t) e^{-\mathrm{i}\omega t}\, \mathrm{d}t. \tag{3}$$

In Section 5, we also present the semi-analytic approach applicable only to the special 3-D models of multiple eccentrically nested spheres (Martinec 1998). For the sake of completeness, we quickly mention its basic features here. The solution of the EM induction equation in each of the homogeneous spheres is expanded into series of vector spherical harmonics and spherical Bessel functions in local coordinate system. Translation formulas are then used to transform all series into one common coordinate system. The continuity of magnetic field across internal interfaces leads to a system of linear equations for the expansion coefficients that is solved directly by Gaussian elimination.

2.4 Integral Equations (IE)

The results from three 'global' numerical solutions which are based on an integral equation with contracting kernel [hereinafter denoted

as contracting integral equation (CIE)] are discussed in the paper. What follows is a summary of the evolution of the CIE concept with a special emphasis on the results relevant to global quasi-3-D (thin sheet) and fully 3-D EM modelling.

The concept was first introduced by Fainberg & Zinger (1980), who obtained an IE of a specific form and proved that this equation can be solved using a simple iterative scheme that always converges to the equation solution. The authors called this technique iterative dissipative method (IDM) and showed that the optimal convergence rate of the IDM iterates is inversely proportional to the lateral contrast of the conductivity distribution. Using IDM Fainberg *et al*. (1990) developed a numerical solution which allowed for calculating EM field in a spherical Earth's model with surface conducting thin sheet and 1-D section underneath.

Singer (1995) derived a new CIE and showed that the optimal convergence rate of simple iterates as applied to new integral equation is inversely proportional to the square root of the lateral contrast of the conductivity distribution. He called this technique modified iterative dissipative method (MIDM). Two remarks are relevant at this point: (i) originally in both methods displacement currents are ignored and only isotropic conductivities are considered; (ii) in both methods optimal convergence rate is achieved by specific choice of the 'reference' 1-D media which does not have to always coincide with the background 1-D section.

Pankratov *et al*. (1995, 1997) [and independently Singer & Fainberg (1995, 1997)] generalized the technique to media with complex-valued conductivities (to account for displacement currents and polarization effects), and to media with tensor-valued conductivities (to account for conductivity anisotropy). In addition, Pankratov *et al*. (1995) proposed a general scheme to construct reference 1-D media which delivers optimal convergence rate, irrespective of whether the conductivity is a real- or complex-valued function. Also Pankratov *et al*. (1995) observed that the simple iterative scheme applied to solve CIE equation can be considered as a partial sum of convergent Neumann series for this equation. In their nomenclature the technique has been named a modified Neumann series (MNS). Kuvshinov *et al*. (1999) implemented the MIDM-MNS concept to 'spherical surface thin sheet' numerical solution and reported—as it was theoretically predicted—the significant improvement in the solution's efficiency.

With regards to the spherical (global) EM modelling using CIE, the next step forward has been done independently by Koyama *et al*. (2002) and Kuvshinov *et al*. (2002) who presented MIDM-MNS numerical solutions which allowed for calculating EM field in fully 3-D earth models. Note that their solutions differ in many aspects: for example, they exploit different strategies for computing the dyad Green's functions. Unfortunately both publications paid little attention to the details of the methods employed to derive and calculate Green's tensors, which are cornerstone components of any IE solution. Only recently Kuvshinov & Semenov (2012) and Koyama *et al*. (2013) published the omitted technical details for their respective solutions (see appendices in these papers).

Further development of CIE approach was made by Avdeev *et al*. (2000), who observed that the integral operator of CIE is well conditioned irrespective of the physically feasible conductivity contrasts, and suggested that Krylov subspace iterates are used to replace the Neumann series summation in the solution of the CIE. Later it was widely reported (Avdeev *et al*. 2002; Kuvshinov *et al*. 2005; Singer 2008) that the implementation of Krylov subspace iterates further reduces a number of iterations needed to obtain the CIE solution. Although it was not proved theoretically, the common observation was that the rate of convergence—if Krylov subspace iterates are implemented—becomes inversely proportional to the 'natural logarithm of the lateral contrast' of the conductivity distribution (see e.g. Singer 2008). Now all codes based on CIE—either working in spherical (Koyama *et al*. 2006; Kuvshinov 2008; Sun & Egbert 2012) or Cartesian (Avdeev *et al*. 2002; Hursan & Zhdanov 2002; Koyama *et al*. 2008; Singer 2008; Avdeev & Knizhnik 2009) geometries—exploit Krylov subspace iterates. In this paper the results from the CIE codes by Koyama *et al*. (2006, KOY), Kuvshinov (2008, KUV) and Sun & Egbert (2012, SUN) are discussed. The first two codes (referred to later in the text as KOY and KUV codes, respectively) are fully 3-D, whilst the code by Sun & Egbert (2012, SUN) deals with the surface thin sheet model which is very similar to the model considered by Fainberg *et al*. (1990) and Kuvshinov *et al*. (1999).

3 MODEL 1: THIN SHELL CONDUCTANCE CONTRAST NS

3.1 Model description and setup

A NS surface or nested hemisphere model has been previously employed to assess computational accuracy (e.g. Kuvshinov *et al*. 1999; Uyeshima & Schultz 2000; Koyama *et al*. 2002; Yoshimura & Oshiman 2002; Sun & Egbert 2012) and is therefore a convenient starting point for numerical comparison in our benchmark exercise. Its sharp discontinuity at the equator allows us to assess the effect of numerical approximations and truncation on the modelling of sharp contrasts. Because of the azimuthal symmetry of both the model and P_1^0 source, the EM response is purely inductive, with no galvanic effects and induced currents aligned parallel to conductivity boundaries. This results in $B_\phi = 0$ for all azimuths ϕ.

The surface NS Hemisphere model consists of a radially symmetric Earth with a (nominally) infinitely thin sheet of non-uniform conductance located at the Earth's surface. The radial conductivity distribution beneath the thin sheet is presented in Table 2.

The shell conductance is 20 000 S in the Northern Hemisphere (colatitudes 0–90°) and 20 S in the Southern Hemisphere (colatitudes 90–180°). The model is longitudinally symmetric. Numerical discretization of this model requires a thin but finite layer of grid cells, typically of the order of 10–50 km thick.

3.2 Results

We obtained results for the NS Hemisphere model from all solvers. Since the models and results are longitudinally symmetric, we present a single profile through zero longitude at the periods of 6 hr and at 4 d in Figs 1 and 2, respectively.

It is notable that there is overall a remarkable agreement between these disparate methods. As expected, SHFE methods [VEL and MAR] exhibit some oscillatory behaviour known as Gibbs phenomenon (also known as ringing, e.g. Figs 1a and b), particularly as the fields approach the sharp NS discontinuity. These methods are also having a harder time resolving the discontinuity itself

Table 2. Radial background conductivity model used as a base for models 1 and 2.

Depths (km)	Conductivities (S m^{-1})
0–100	0.0001
100–400	0.01
400–650	0.1
650–6371.2	2

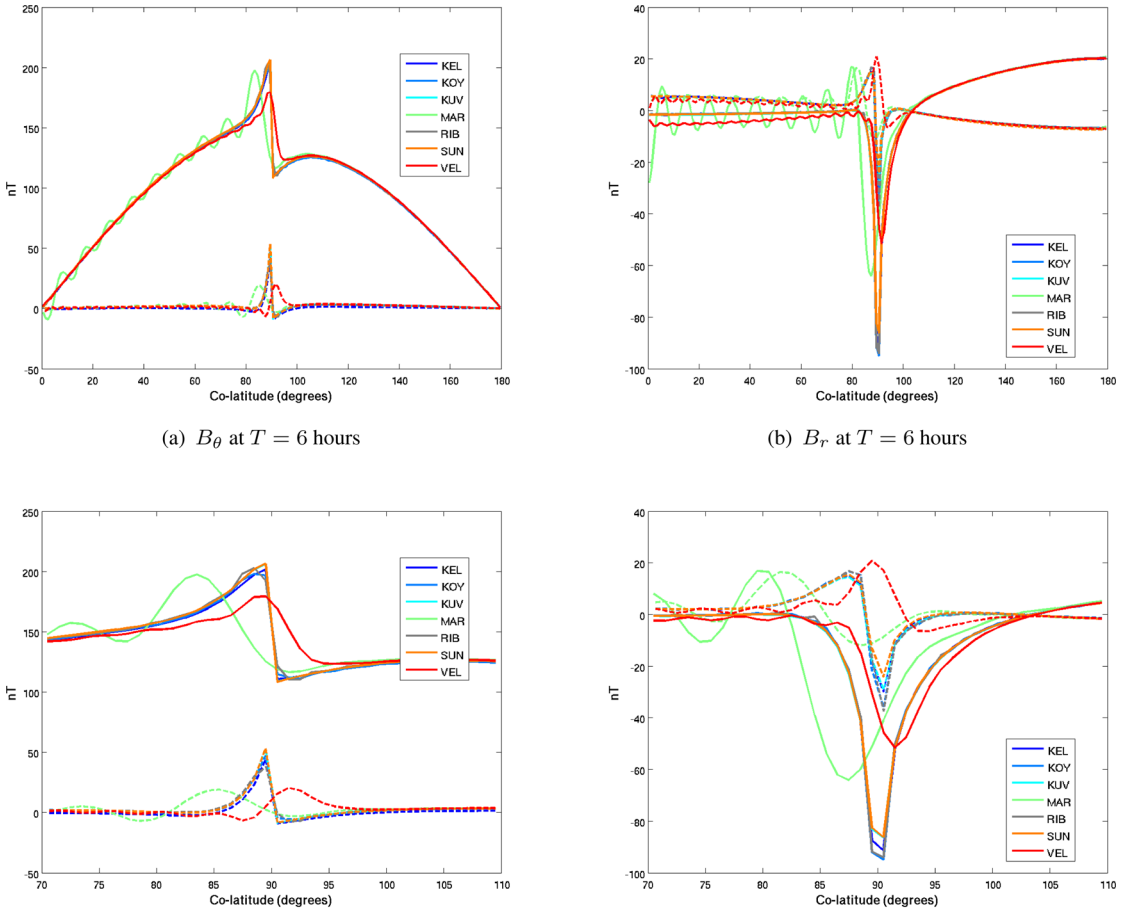

(a) B_θ at $T = 6$ hours

(b) B_r at $T = 6$ hours

(c) B_θ at $T = 6$ hours: close up

(d) B_r at $T = 6$ hours: close up

Figure 1. A subset of magnetic field profiles for benchmark case 1: North/South Hemispheres at period $T = 6$ hr. Solid lines are utilized for real components of the magnetic fields; dashed lines are the imaginary components.

(e.g. close-ups in Figs 1c and d). Other methods resolve the NS discontinuity well.

4 MODEL 2: THIN SHELL CONDUCTANCE CONTRAST WEST/EAST

4.1 Model description and setup

It is useful to consider a setup very similar to that discussed in the previous section, with the discontinuity passing through the poles, rather than aligned with the Earth's equator. The P_1^0 source approximation, adopted by us for this benchmark comparison (common also in the majority of global induction studies to date) favours a longitudinally symmetric geometry. This benchmark case is therefore quite distinct from the one discussed in the previous section. Moreover, many spherical forward solvers have singularities at the Earth's poles, which could be an additional source of numerical errors.

Just like the North/South Hemispheres, the surface West/East (WE) Hemisphere model consists of a radially symmetric Earth with an infinitely thin sheet of non-uniform conductance located at the Earth's surface. The radial conductivity distribution is as in Table 2. The shell conductance is 20 S at longitudes 0–90°, 20 000 S at longitudes 90–270° and again 20 S at longitudes 270–360°. The model of latitudinally symmetric. This setup has also been previously employed for assessing numerical accuracy of 3-D solutions (e.g. Kuvshinov *et al*. 2005; Sun & Egbert 2012).

4.2 Results

Similarly to Section 3, we obtained the results for the WE hemisphere model at four periods (6 hr, 1, 4 and 16 d) using the solvers KEL, KOY, KUV, MAR, RIB, SUN and VEL. While the model is defined in the same way across all latitudes, the spherical nature of the model and a P_1^0 source makes the results fully 3-D. Therefore, we try to present them as thoroughly as possible.

Like model 1, model 2 is also a native setup for IE solvers KOY, KUV and SUN. As expected, these solvers perform very consistently, with variations of no more than a few nT located in just a few grid cells contouring the corners of the embedded thinsheet conductor. At a relatively high computational expense (see Section 9), the FD solver KEL is able to perform just as accurately as the IE solvers for this modelling setup.

Like in Section 3, an oscillatory behaviour of SHFE methods [VEL and MAR] is again a striking feature of the solutions (Figs 3

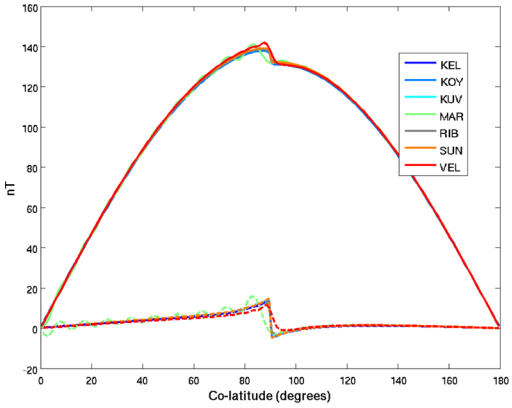

(a) B_θ at $T = 4$ days

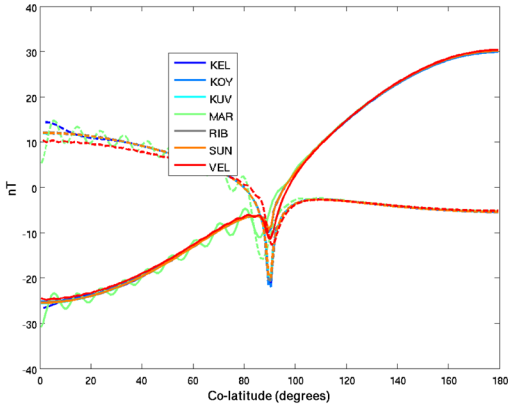

(b) B_r at $T = 4$ days

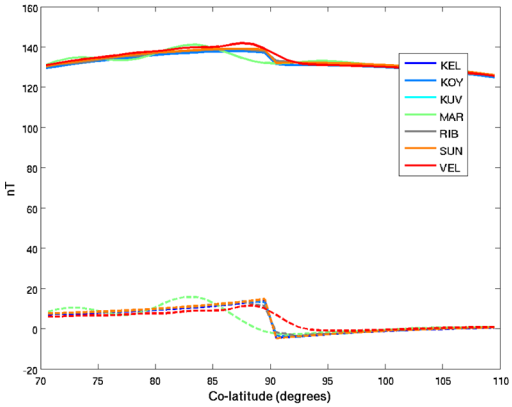

(c) B_θ at $T = 4$ days: close up

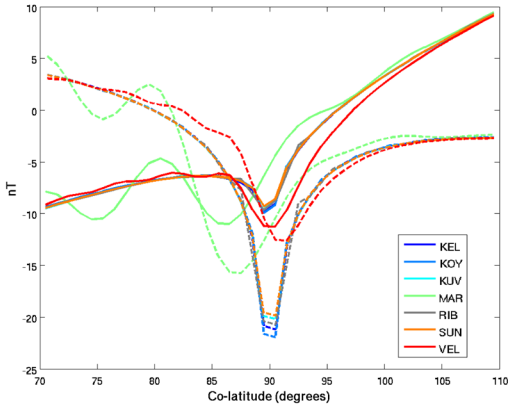

(d) B_r at $T = 4$ days: close up

Figure 2. A subset of magnetic field profiles for benchmark case 1: North/South Hemispheres at period $T = 4$ d. Solid lines are utilized for real components of the magnetic fields; dashed lines are the imaginary components.

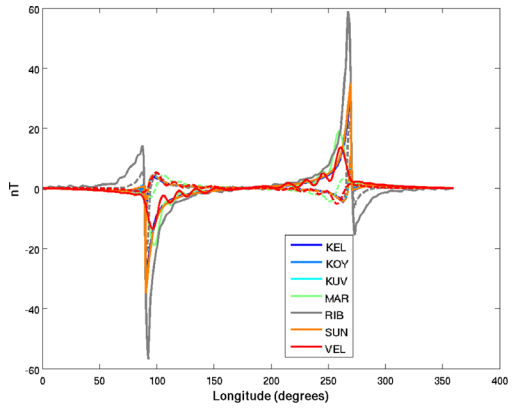

(a) B_ϕ at $\theta = 45.5°, T = 6$ hours

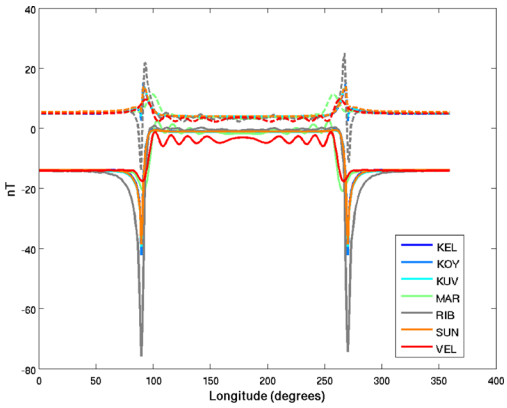

(b) B_r at $\theta = 45.5°, T = 6$ hours

Figure 3. A subset of magnetic field profiles for benchmark case 2: West/East Hemispheres at $T = 6$ hr. These latitudinal profiles consistently resolve the boundaries of the conductive anomaly. Solid lines are utilized for real components of the magnetic fields; dashed lines are the imaginary components.

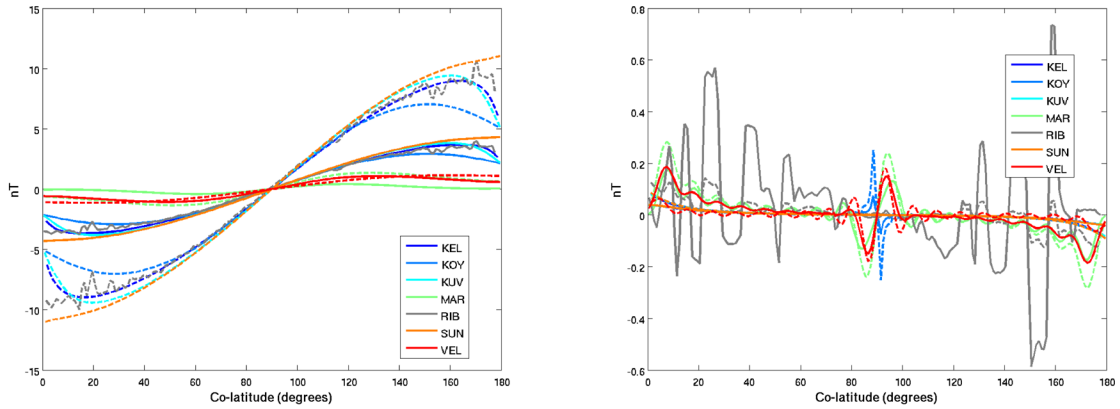

(a) B_ϕ at $\phi = 90.5°$ (b) B_ϕ at $\phi = 180.5°$

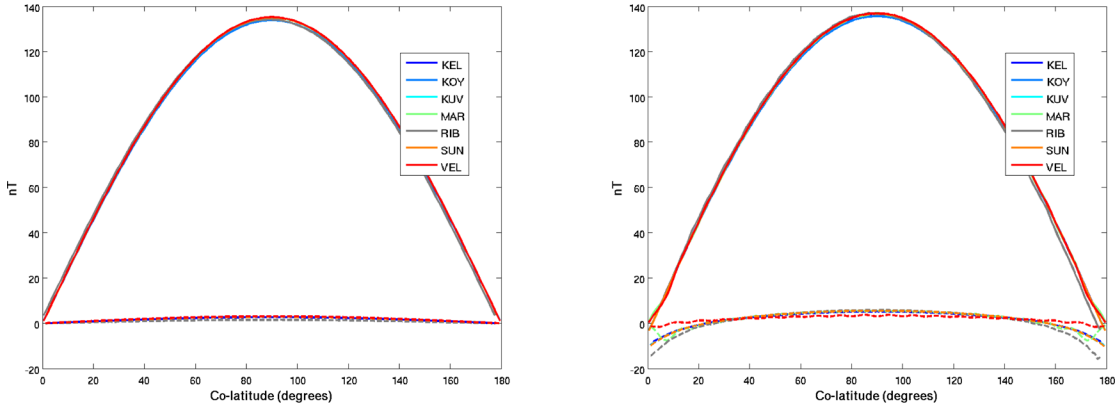

(c) B_θ at $\phi = 90.5°$ (d) B_θ at $\phi = 180.5°$

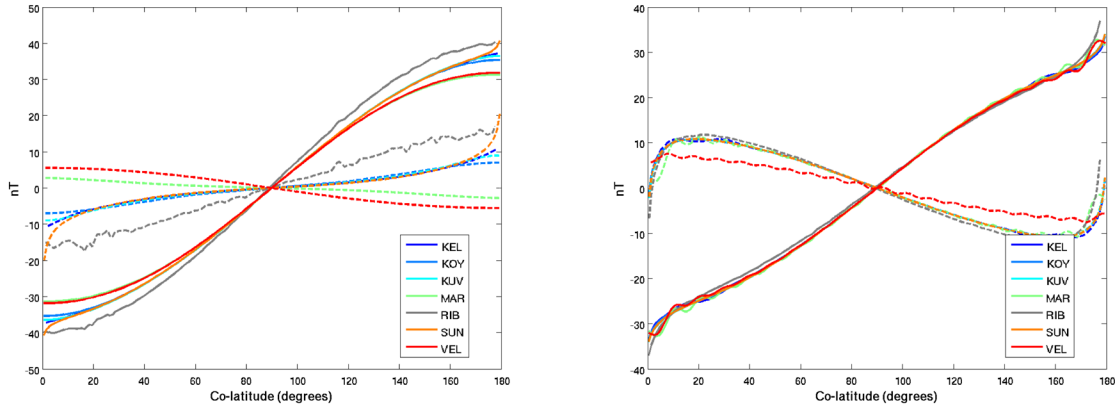

(e) B_r at $\phi = 90.5°$ (f) B_r at $\phi = 180.5°$

Figure 4. A subset of magnetic field profiles for benchmark case 2: West/East Hemispheres at $T = 4$ d, plotted at the first grid cells after 90° and 180° longitude for error analysis. Solid lines are utilized for real components of the magnetic fields; dashed lines are the imaginary components.

and 4). However, other features also appear, particularly the errors at the corners and extending all along the boundaries of the conductive anomaly (Figs 5–7). These are most notable in the SHFE solvers MAR and VEL and the FE solver RIB, sometimes reaching the magnitudes comparable to the amplitudes of the solutions. However, all solvers exhibit reasonable consistency at the poles (Fig. 4) and in the large-scale structure (Figs 5–7).

5 MODEL 3: ECCENTRICALLY NESTED SPHERE

5.1 Model description and setup

An axially asymmetric, eccentrically nested sphere embedded deep in the Earth's mantle is a particularly interesting benchmark

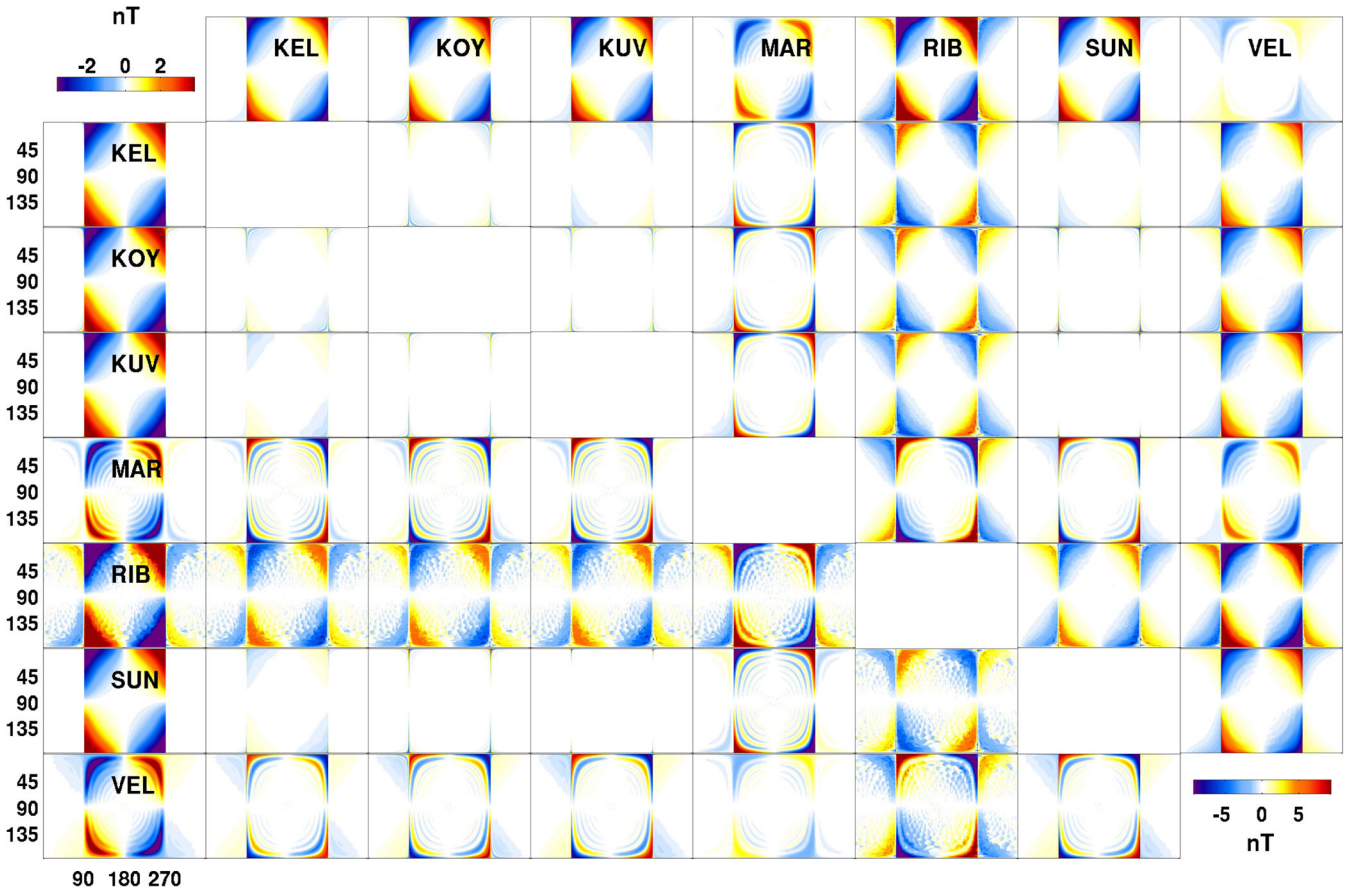

Figure 5. Real and imaginary parts of the ϕ-component of the magnetic field for benchmark case 2 at a single period (4 d). The first (vertical) column corresponds to the real part of the magnetic fields. The colourbar at the top corresponds to the real part. The first (horizontal) row is the imaginary part. The colourbar at the bottom corresponds to the imaginary part. The lower triangle are the differences between the real parts from different codes. The upper triangle are the differences between the imaginary parts from different codes. The diagonal is empty. The colour scales used for the differences have the same ranges as the corresponding real/imag parts but they are shifted to be centred around zero.

example, as the curvilinear contrast presents much difficulty for numerical modelling, particularly when a structured grid is employed. It is also one of the most useful test cases, since it is arguably the most complicated example for which a semi-analytic solution exists (Martinec 1998).

The setup of this model is as described in Fig. 8. The background sphere K_1 (which models the Earth) has radius 6731 km and conductivity 0.01 S m^{-1}. The spherical inclusion K_2 has radius 1200 km and conductivity 1.00 S m^{-1}. The centre O_2 of the inclusion is shifted with respect of the centre O_1 of the sphere K_1 by distance of $d_1 = 4921$ km in the direction of colatitude $\vartheta_1 = 40^\circ$ and longitude $\varphi_1 = 35^\circ$. In terms of depths, the smaller spherical inclusion spans from 250 to 2650 km depth with centre 1450 km deep.

5.2 Results

Six solvers attempted this model setup: KEL, KOY, KUV, MAR, RIB and VEL (Figs 9–12). In addition, a semi-analytic solution based on Martinec (1998) is also shown.

All models are able to reproduce the semi-analytic curves in Fig. 9 with various precision. At the relatively high accuracy level and the related computational costs employed by KEL for this model (see Section 9), it is able to very accurately reproduce the semi-analytic peaks/troughs caused by the embedded spherical anomaly (see also Figs 10–12). This illustrates the inherent ability of even a structured finite difference grid to model any complicated geometry. However, the real part of the B_θ component is somewhat underestimated by KEL, and the imaginary part overestimated (see Fig. 11). Interestingly, this bias is inherent to KEL FWD modelling. Our numerical experiments show that this bias disappears completely when secondary field formulation is employed. We speculate that the bottom boundary conditions are affecting the magnitude of B_θ.

Although there is general agreement in the character of the B_ϕ response, results are consistent to within a few nT. The modelling of RIB gives rise to non-local instabilities and perhaps requires additional stabilization.

6 MODEL 4: BURIED BLOCK

6.1 Model description and setup

Here, we consider a somewhat more complicated example which incorporates the sharp edges of Models 1 and 2 and the fully 3-D nature of Model 3. Specifically, we define a conductive buried

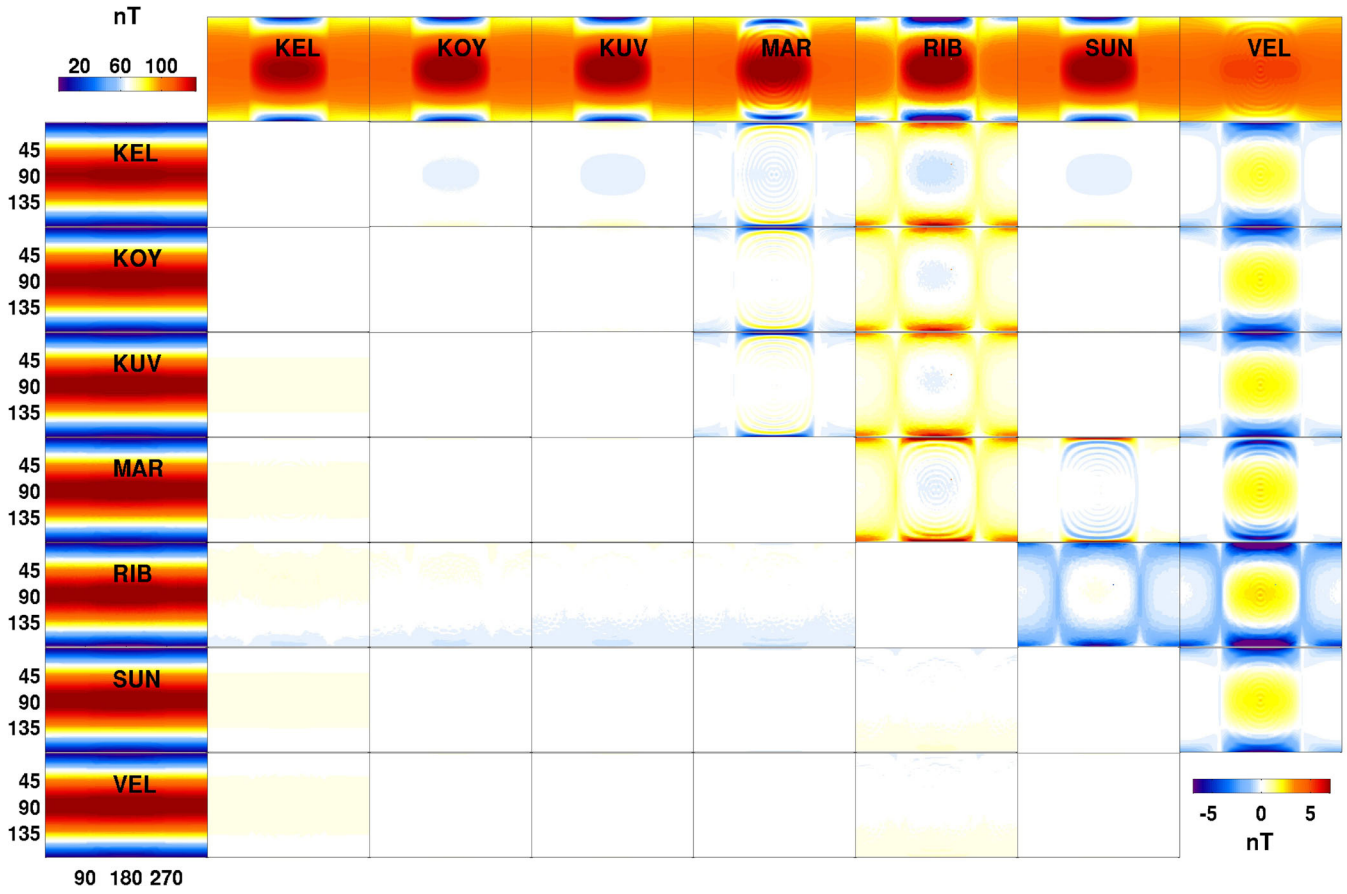

Figure 6. Real and imaginary parts of the θ-component of the magnetic field for benchmark case 2 at a single period (4 d). The first (vertical) column corresponds to the real part of the magnetic fields. The colourbar at the top corresponds to the real part. The first (horizontal) row is the imaginary part. The colourbar at the bottom corresponds to the imaginary part. The lower triangle are the differences between the real parts from different codes. The upper triangle are the differences between the imaginary parts from different codes. The diagonal is empty. The colour scales used for the differences have the same ranges as the corresponding real/image parts but they are shifted to be centred around zero.

block in a radially symmetric mantle, at approximately transition zone depths (Table 3). The $30^\circ \times 30^\circ$ anomaly is placed in the second host layer (in equatorial region) and has conductivity of 1 S m^{-1} as described in Table 4. The P_1^0 source excitation and periods are as in Sections 3–5.

6.2 Results

Five solvers attempted the solution: KEL, KOY, KUV, MAR and VEL. The results are presented in Figs 13–16. In the B_θ components, the FD solver KEL and the IE solver KOY exhibit most similarity between themselves, with only minor differences (2 nT in the real part and 0.5 nT in the imaginary part) localized in the area of the nested block anomaly. Source dominated differences of up to ± 5 nT in the real part and up to ± 1 nT in the imaginary part are observed between this cluster, and the KUV, MAR and VEL solutions. In the radial component B_r, all solutions exhibit great similarity, with most notable deviations up to ± 4 nT in the real part and ± 2 nT in the imaginary part arising at the upper and lower boundaries of the embedded block. The only exception is KOY solver, which exhibits a minor source dependent deviation from the other solutions in B_r. All B_ϕ solutions are similar in character but exhibit local variations in the magnitudes of the solutions of the order of up to ± 1 nT.

7 MODEL 5: SPHERICAL HARMONICS OF VARIED DEGREES AND ORDERS

7.1 Model description and setup

Spherical harmonic model representations come naturally to techniques like SHFE methods. However, they are expected to present the most technical difficulties to integral equation methods which are most naturally suited to localized anomalies and sharp discontinuities.

Here, we define three spherical harmonic perturbation settings:

(i) $l = 2$ $m = +2$ coefficient set to +1.2
(ii) $l = 6$ $m = +4$ coefficient set to +1.7
(iii) $l = 12$ $m = +8$ coefficient set to +2.2,

where the values are expressed as $\log_{10}(\sigma)$, σ being the electrical conductivity in S m^{-1}. We have chosen the Schmidt semi-normalized spherical harmonic parametrization, and the coefficients are such that when the spherical harmonic perturbations are mapped

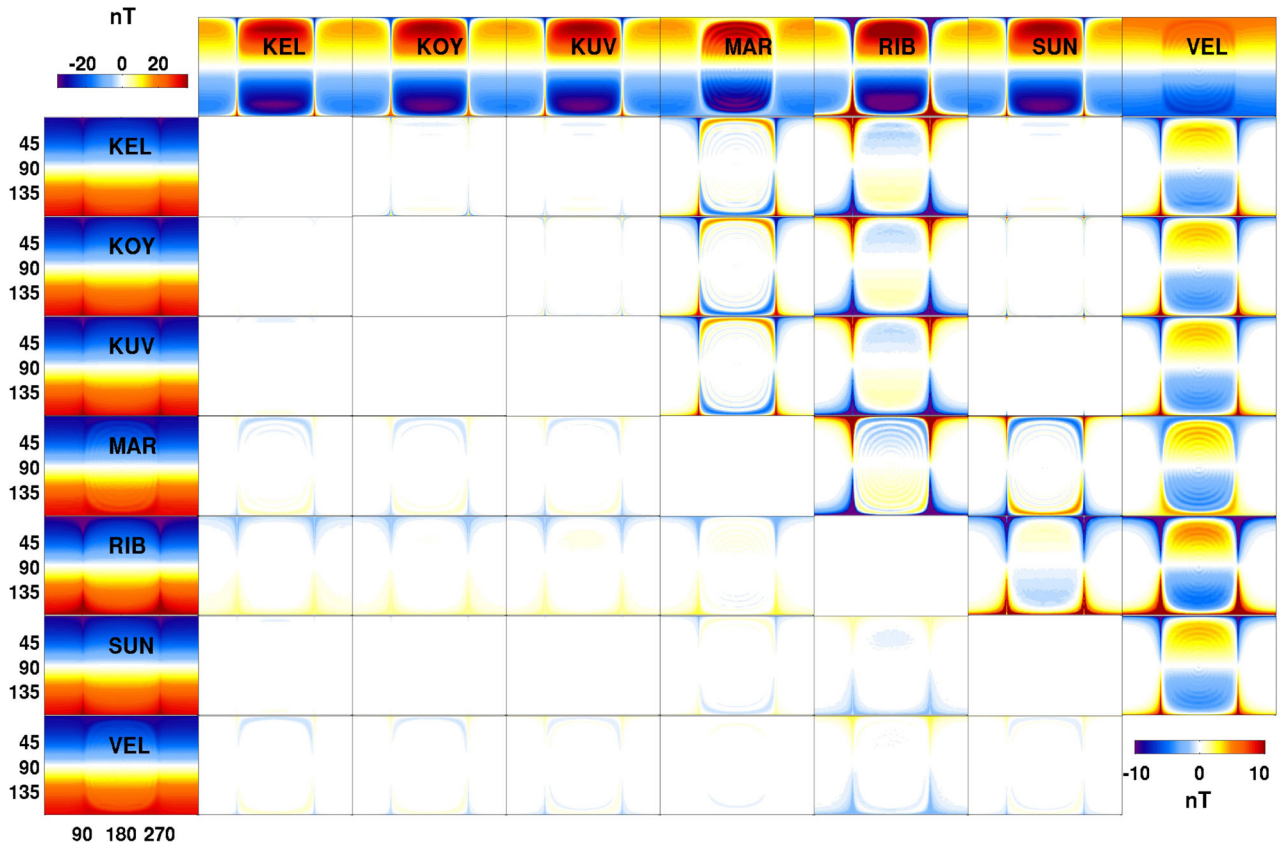

Figure 7. Real and imaginary parts of the radial component of the magnetic field for benchmark case 2 at a single period (4 d). The first (vertical) column corresponds to the real part of the magnetic fields. The colourbar at the top corresponds to the real part. The first (horizontal) row is the imaginary part. The colourbar at the bottom corresponds to the imaginary part. The lower triangle are the differences between the real parts from different codes. The upper triangle are the differences between the imaginary parts from different codes. The diagonal is empty. The colour scales used for the differences have the same ranges as the corresponding real/imag parts but they are shifted to be centred around zero.

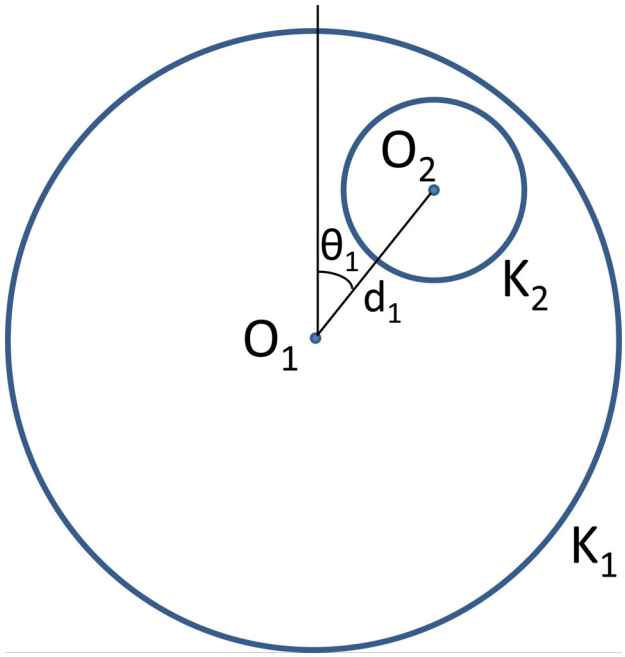

Figure 8. Nested sphere model setup. Schematic adapted from Martinec (1998).

to a grid, the peaks correspond to just over ± 1 ($\log_{10}$ scale) (see Fig. 17). So the total variations are ∼two orders of magnitude. These perturbations are defined in the layer 400–650 km, replacing the relevant layer in the 1-D host as in Table 2. The P_1^0 source excitation and periods are as in Sections 3–6.

The rationale for making the three examples so distinctly different is as follows. Degree 2 example is a basic test of modelling with smooth conductivity variations; this example is conceptually comparable to 3-D nested spheres or a blocky anomaly. Degree 6 variations should be easily visible in the magnetic fields, and clearly resolvable with a reasonable synthetic data distribution, making it an ideal case study for possible future synthetic inversion benchmark and tests. Finally, degree 12 is a great example for exploring our spatial limitations. The diameter of degree 12 order 8 anomalies is approximately 20°, and this is where our resolution restrictions start making a difference (for example, a $5^\circ \times 5^\circ$ grid would produce a misleading representation of these anomalies). Anomalies at this scale should be at the verge of our spatial resolution with existing global data sets, and present computational resources. In addition, this model set is explored as groundwork for a global EM inversion benchmark study (in preparation). To this end, we anticipate degree 12 to provide a good test case to assess spatial resolution and adequacy of lateral regularization.

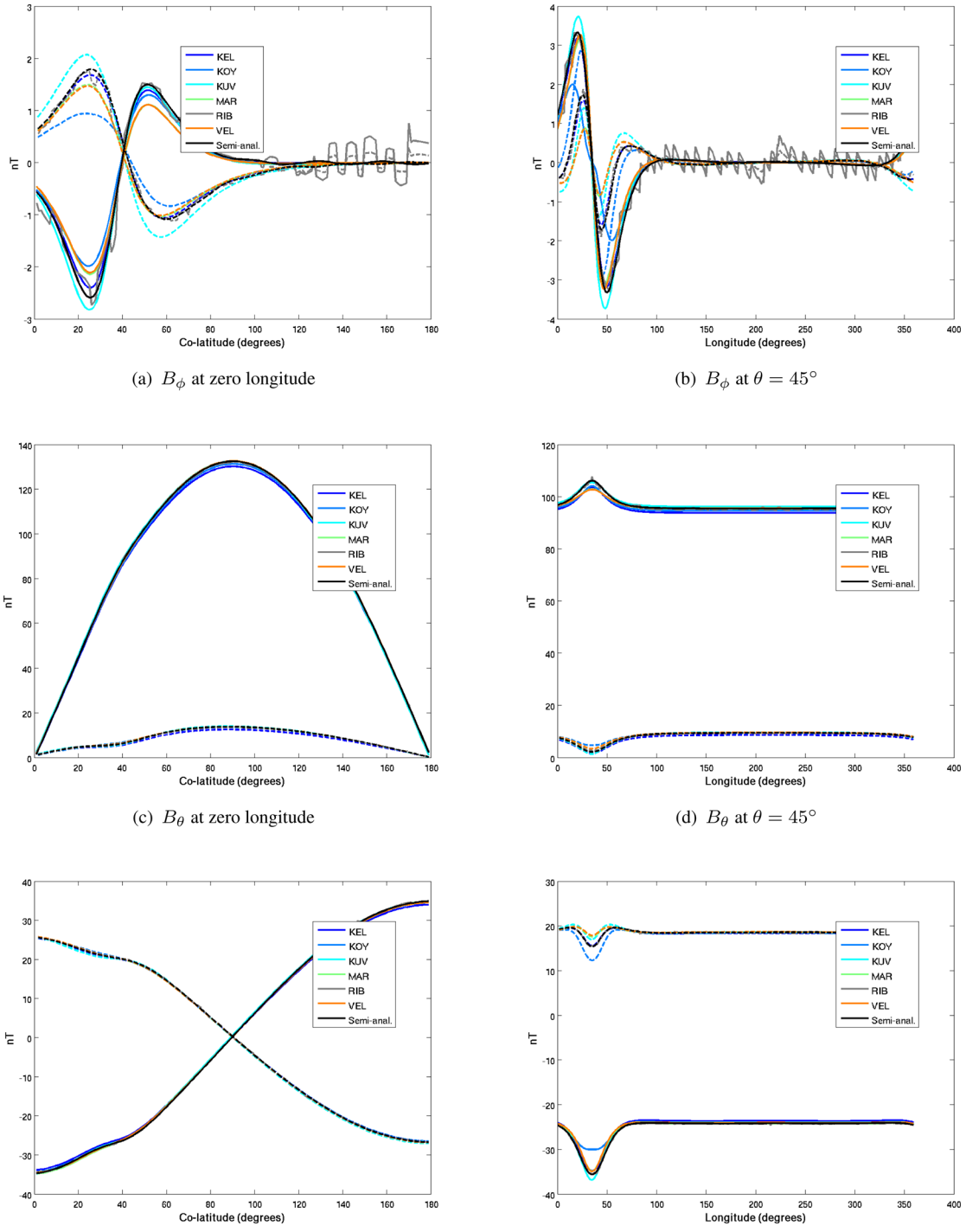

(a) B_ϕ at zero longitude

(b) B_ϕ at $\theta = 45°$

(c) B_θ at zero longitude

(d) B_θ at $\theta = 45°$

(e) B_r at zero longitude

(f) B_r at $\theta = 45°$

Figure 9. A subset of magnetic field profiles for benchmark case 3: embedded sphere at $T = 1$ d. Solid lines are utilized for real components of the magnetic fields; dashed lines are the imaginary components.

7.2 Results

Five solvers attempted the solution: KEL, KOY, KUV, MAR and VEL. Sample cross-comparisons of the results are presented in Figs 18–26. Geomagnetic induction occurs in the presence of interconnected conductors. Thus, the spherical harmonic checkerboard patterns present an especially difficult exercise for electromagnetic modelling. Here, we show the cross-comparison between the radial, θ and ϕ components of the magnetic field at a sample period of 4 d, for all three spherical harmonic models.

Large scale structure allow for greater similarities between the solutions. For example, for the simplest $l = 2$ $m = 2$

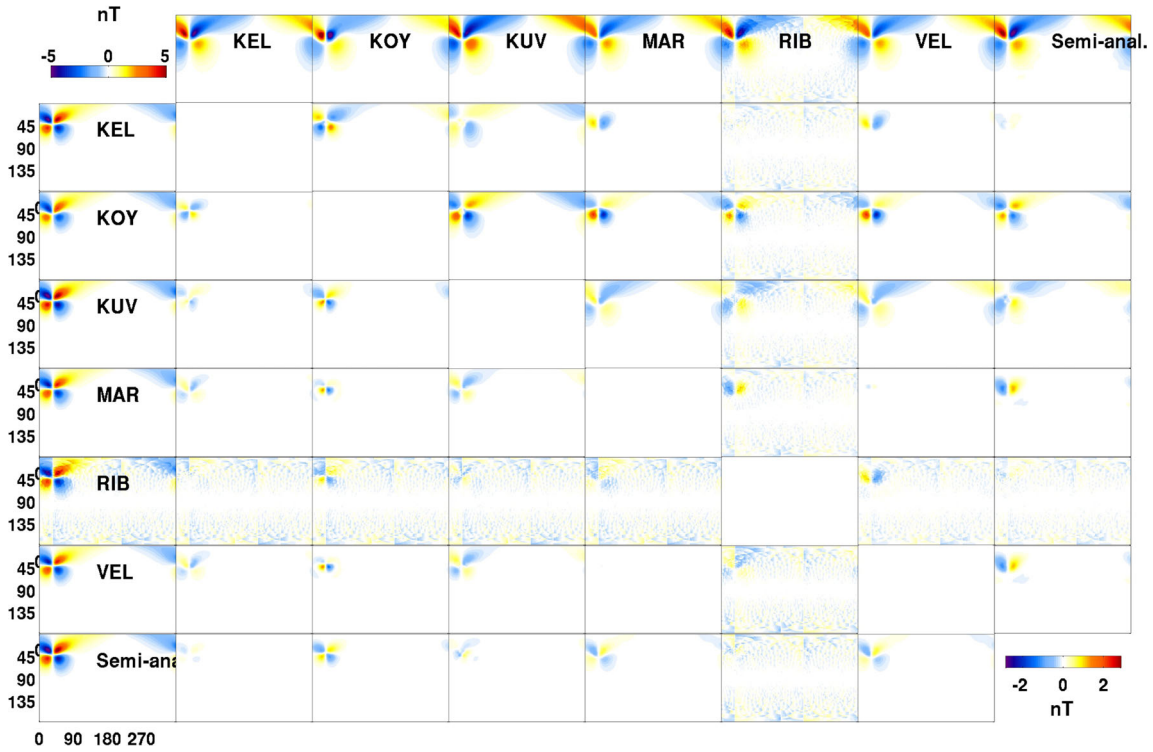

Figure 10. Real and imaginary parts of the ϕ-component of the magnetic field for benchmark case 3 at a single period (1 d). The first (vertical) column corresponds to the real part of the magnetic fields. The colourbar at the top corresponds to the real part. The first (horizontal) row is the imaginary part. The colourbar at the bottom corresponds to the imaginary part. The lower triangle are the differences between the real parts from different codes. The upper triangle are the differences between the imaginary parts from different codes. The diagonal is empty. The colour scales used for the differences have the same ranges as the corresponding real/imag parts but they are shifted to be centred around zero.

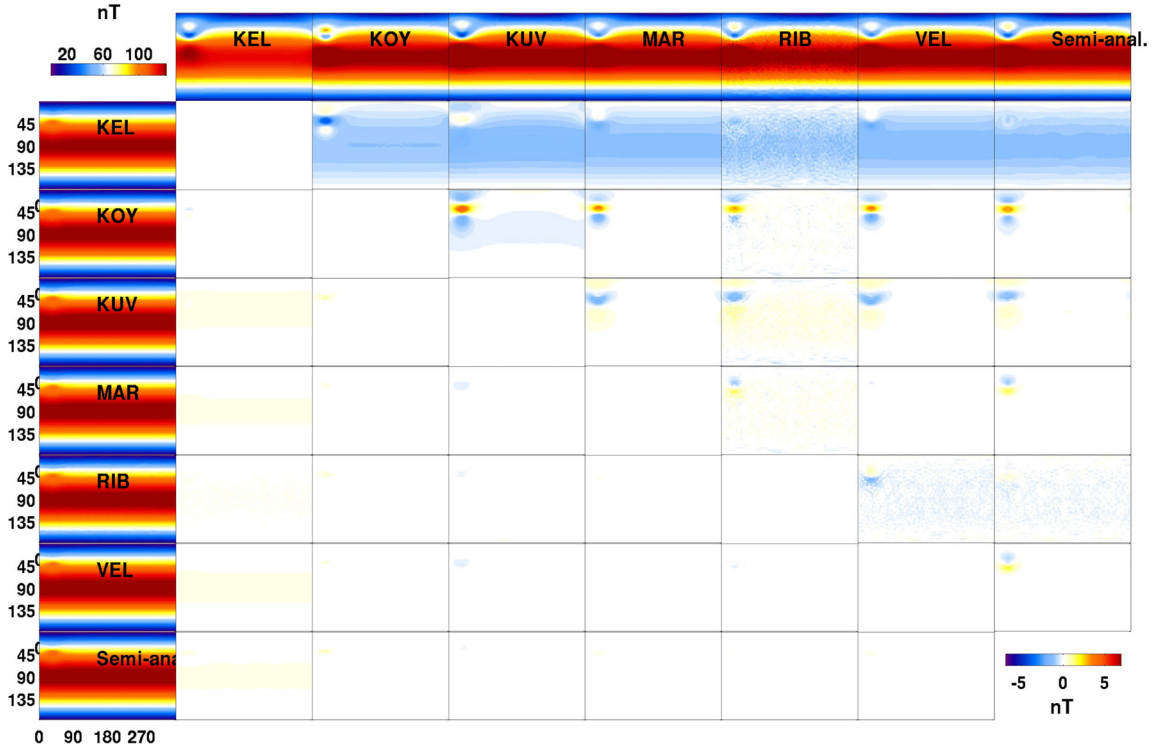

Figure 11. Real and imaginary parts of the θ-component of the magnetic field for benchmark case 3 at a single period (1 d). The first (vertical) column corresponds to the real part of the magnetic fields. The colourbar at the top corresponds to the real part. The first (horizontal) row is the imaginary part. The colourbar at the bottom corresponds to the imaginary part. The lower triangle are the differences between the real parts from different codes. The upper triangle are the differences between the imaginary parts from different codes. The diagonal is empty. The colour scales used for the differences have the same ranges as the corresponding real/imag parts but they are shifted to be centred around zero.

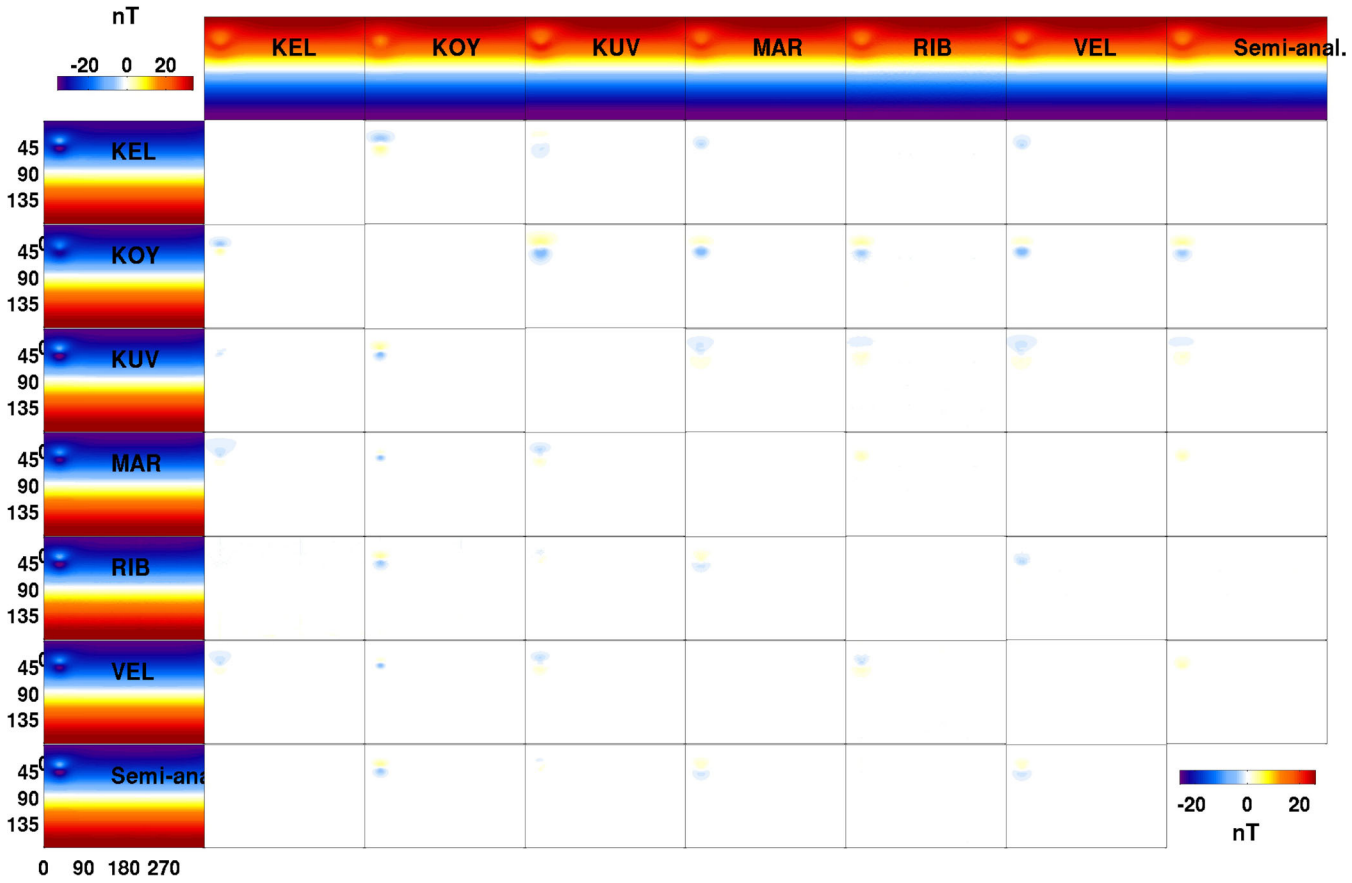

Figure 12. Real and imaginary parts of the radial component of the magnetic field for benchmark case 3 at a single period (1 day). The first (vertical) column corresponds to the real part of the magnetic fields. The colourbar at the top corresponds to the real part. The first (horizontal) row is the imaginary part. The colourbar at the bottom corresponds to the imaginary part. The lower triangle are the differences between the real parts from different codes. The upper triangle are the differences between the imaginary parts from different codes. The diagonal is empty. The colour scales used for the differences have the same ranges as the corresponding real/imag parts but they are shifted to be centred around zero.

Table 3. Radial background conductivity model used as a base for model 4.

Depths (km)	Conductivities (S m^{-1})
0–400	0.004
400–800	0.04
800–6371.2	2

Table 4. Definition of model 4.

Colatitudes	Longitudes	Conductivity
0–75°	0–360°	0.04 S m^{-1}
75–105°	0–165°	0.04 S m^{-1}
75–105°	165–195°	1 S m^{-1}
75–105°	195–360°	0.04 S m^{-1}
105–180°	0–360°	0.04 S m^{-1}

model, the differences in B_r never exceed ± 0.8 nT. In B_θ, the absolute differences are bigger in the real part, reaching up to ± 4 nT, versus less than ± 0.5 nT in the imaginary part. Those in B_ϕ are of the order of ± 0.1–0.2 nT (amounting to up to 8 per cent in the real and 20 per cent in the imaginary part).

The consistency between the solutions is reduced when finer scale structures are introduced. In the extreme case of $l = 12$ $m = 8$, the differences in the B_r component go up to ± 1.5 nT, amounting to $\sim$3 to 6 per cent in the real part and 5–20 per cent in the imaginary part. Similarly, the differences in the imaginary part of B_θ range from 7 to 26 per cent of the field component, while the errors in the real part of B_θ never exceed 3 per cent. The biggest inconsistencies are encountered in the B_ϕ. Maximum differences range from 1 to 15 per cent in the real part of the component; however, in the imaginary component this deviation sometimes amounts to 20–80 per cent of the component value. In both the real and imaginary components of the field, the maximum differences vary from 0.1 to 1 nT; KEL and KOY are more consistent between themselves, with maximum differences being no more than 2 per cent in the real and 20 per cent in the imaginary components. While the absolute differences are not dramatically increased compared to the simpler $l = 2$ $m = 2$ and $l = 6$ $m = 4$ models, the relative errors increase very substantially. We suggest that this is mostly due to the magnitude of the response being diminished when smaller scale conductors are considered. The blueberry–raspberry pie appearance of these plots brings out consistent inaccuracies in our formulations that give us an upper limit on the numerical errors we might encounter.

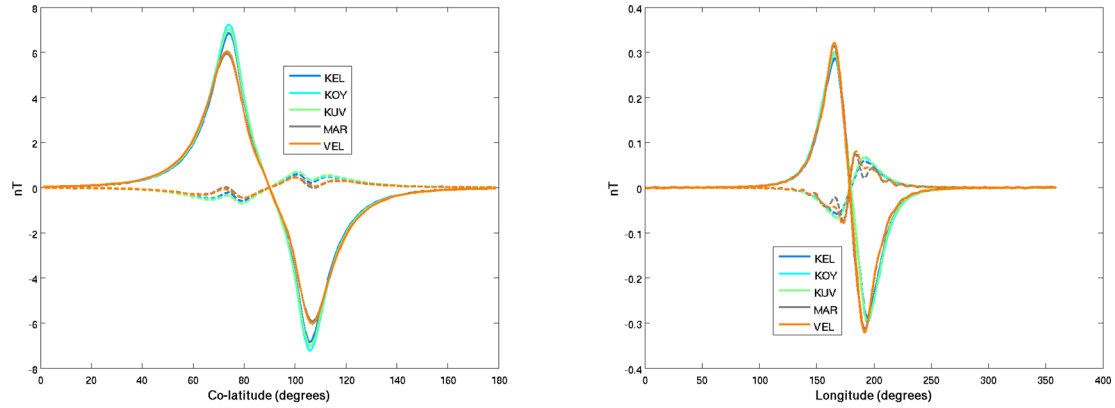

(a) B_ϕ at $\phi = 195°$ (b) B_ϕ at $\theta = 90°$

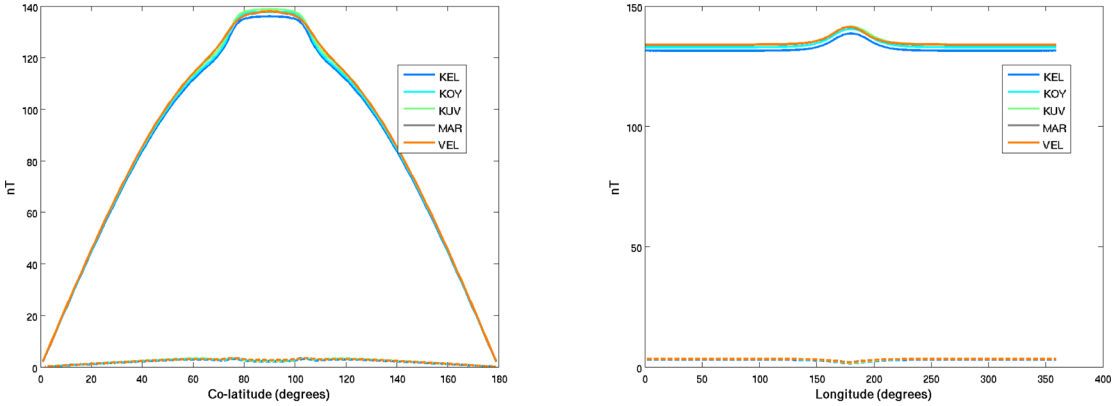

(c) B_θ at $\phi = 195°$ (d) B_θ at $\theta = 90°$

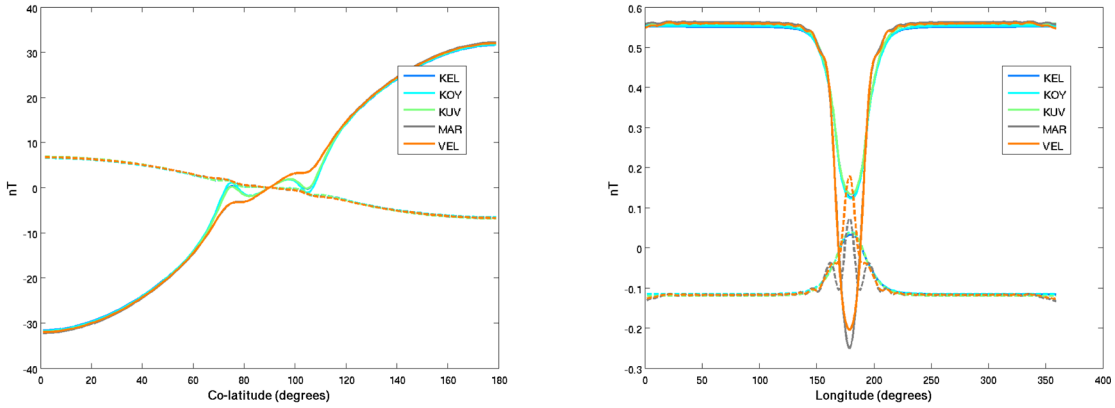

(e) B_r at $\phi = 195°$ (f) B_r at $\theta = 90°$

Figure 13. A subset of magnetic field profiles for benchmark case 4: buried block, plotted at the edge of the block ($\phi = 195°$) and across the centre ($\theta = 90°$) for $T = 1$ d. Solid lines are utilized for real components of the magnetic fields; dashed lines are the imaginary components.

8 MODEL 6: GLOBAL CONDUCTANCE MAP

8.1 Model description and setup

To conclude our study, we compare performance of our solvers on a realistic 3-D surface conductance map (Everett *et al*. 2003) over a radial conductivity model adapted from Medin *et al*. (2007) and described by Table 5. Numerical methods which model the near-surface conductance map explicitly have assumed this conductance to be distributed over 50 km as in Everett *et al*. (2003). As with previous models, all computations were performed in the coordinate system defined by the dipolar geometry of the external field, that is in geomagnetic coordinates. Therefore, the surface conductance

Figure 14. Real and imaginary parts of the ϕ-component of the magnetic field for benchmark case 4 at a single period (1 d). The first (vertical) column corresponds to the real part of the magnetic fields. The colourbar at the top corresponds to the real part. The first (horizontal) row is the imaginary part. The colourbar at the bottom corresponds to the imaginary part. The lower triangle are the differences between the real parts from different codes. The upper triangle are the differences between the imaginary parts from different codes. The diagonal is empty. The colour scales used for the differences have the same ranges as the corresponding real/imag parts but they are shifted to be centred around zero.

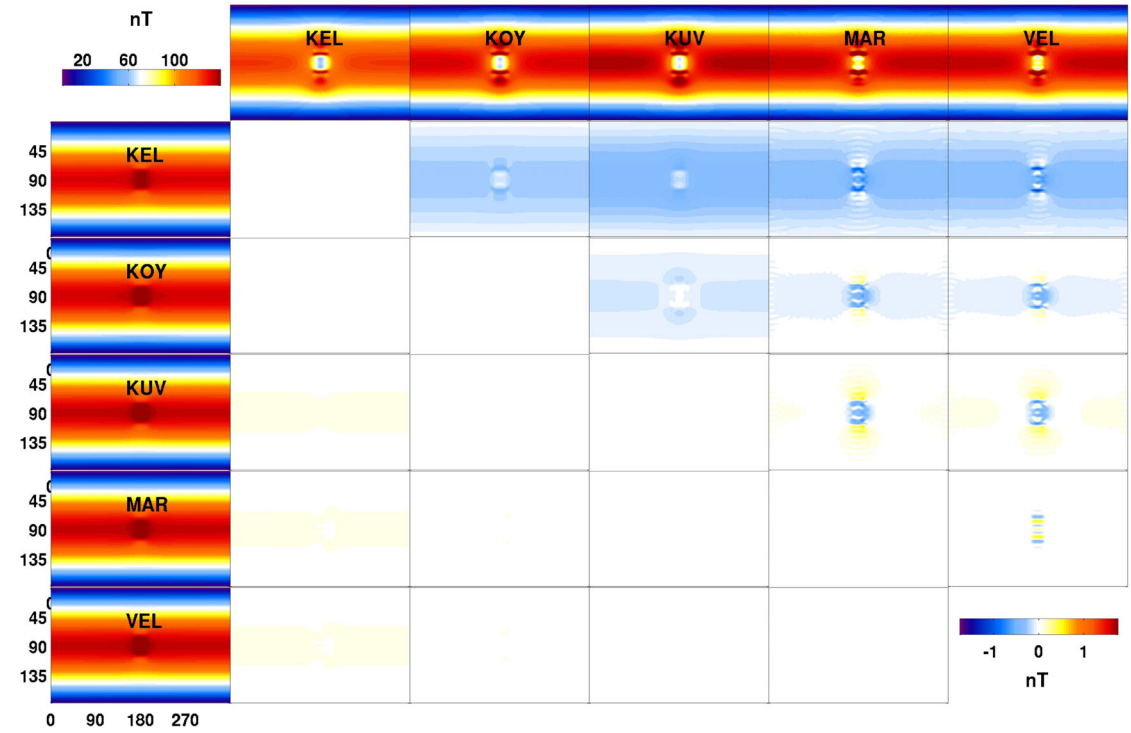

Figure 15. Real and imaginary parts of the θ-component of the magnetic field for benchmark case 4 at a single period (1 d). The first (vertical) column corresponds to the real part of the magnetic fields. The colourbar at the top corresponds to the real part. The first (horizontal) row is the imaginary part. The colourbar at the bottom corresponds to the imaginary part. The lower triangle are the differences between the real parts from different codes. The upper triangle are the differences between the imaginary parts from different codes. The diagonal is empty. The colour scales used for the differences have the same ranges as the corresponding real/imag parts but they are shifted to be centred around zero.

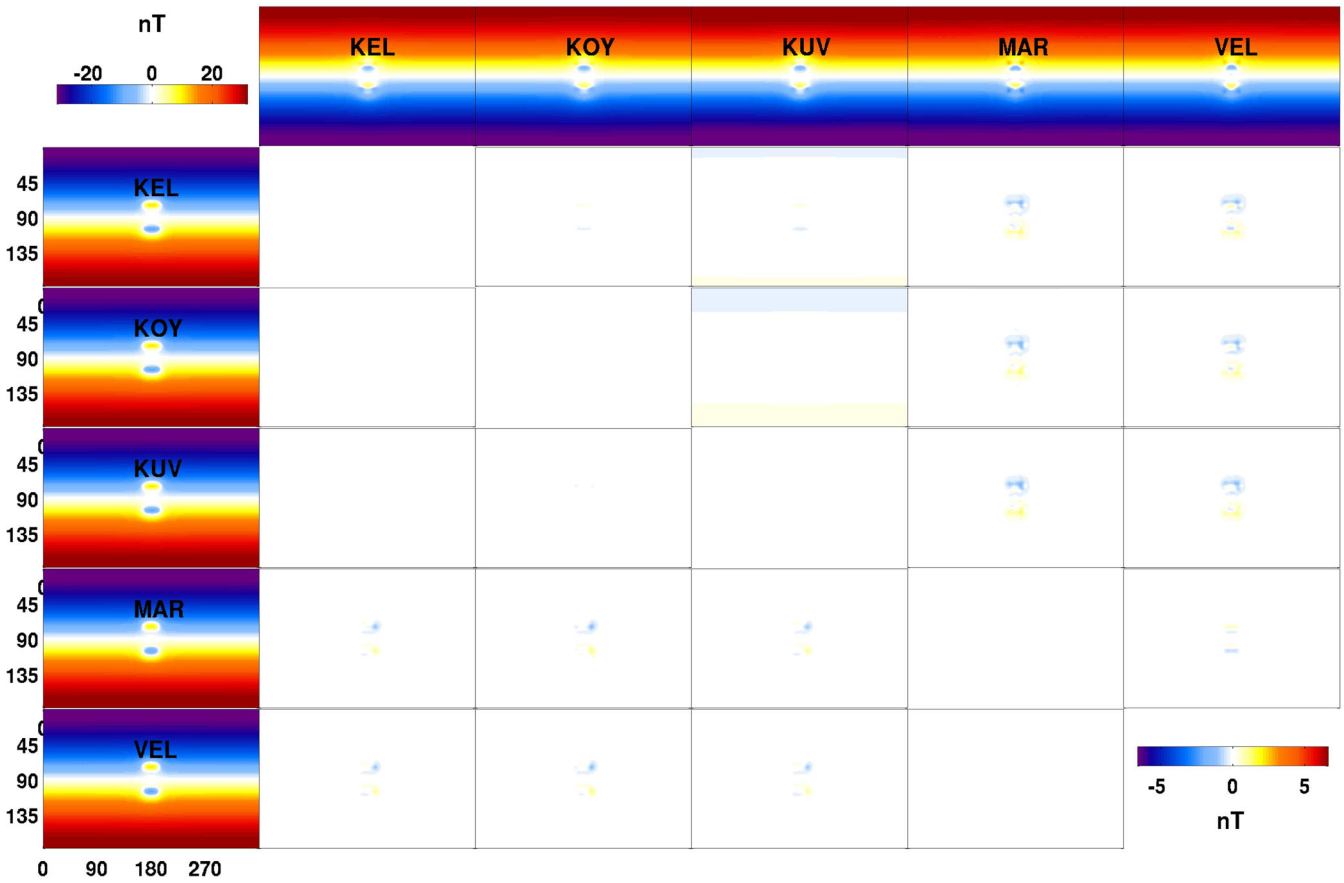

Figure 16. Real and imaginary parts of the radial component of the magnetic field for benchmark case 4 at a single period (1 day). The first (vertical) column corresponds to the real part of the magnetic fields. The colourbar at the top corresponds to the real part. The first (horizontal) row is the imaginary part. The colourbar at the bottom corresponds to the imaginary part. The lower triangle are the differences between the real parts from different codes. The upper triangle are the differences between the imaginary parts from different codes. The diagonal is empty. The colour scales used for the differences have the same ranges as the corresponding real/imag parts but they are shifted to be centred around zero.

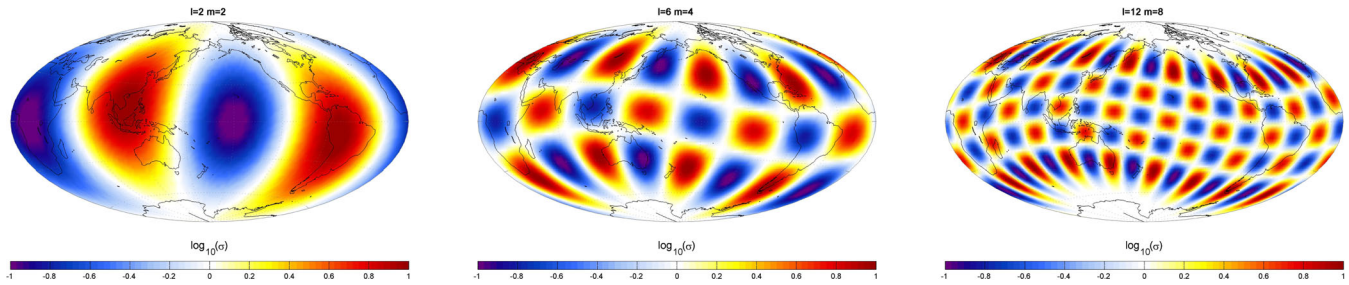

(a) l=2 m=2 (b) l=6 m=4 (c) l=12 m=8

Figure 17. Synthetic model 5: spherical harmonic perturbations. Adapted from Kelbert *et al*. (2008).

map was also rotated into geomagnetic coordinates, and the field components presented here are also expressed in the geomagnetic system.

8.2 Results

All seven solvers attempted the computations for this model. The comparison of the solutions in native geomagnetic coordinates is presented in Figs 27–29. The deviations between the KEL, KOY, KUV and SUN solutions, sometimes reaching ±10–20 nT, are localized in thin stripes around the conductive/resistive boundaries (continent contours). The differences between these codes and MAR and VEL are about twice as big and result from the 'ripple-like' effect of SHFE methods. These are concentrated in the 'conductors'—the oceans. Finally, the deviations of the order of several hundreds of nT of an FE code RIB from the cluster of IE and FD solutions are

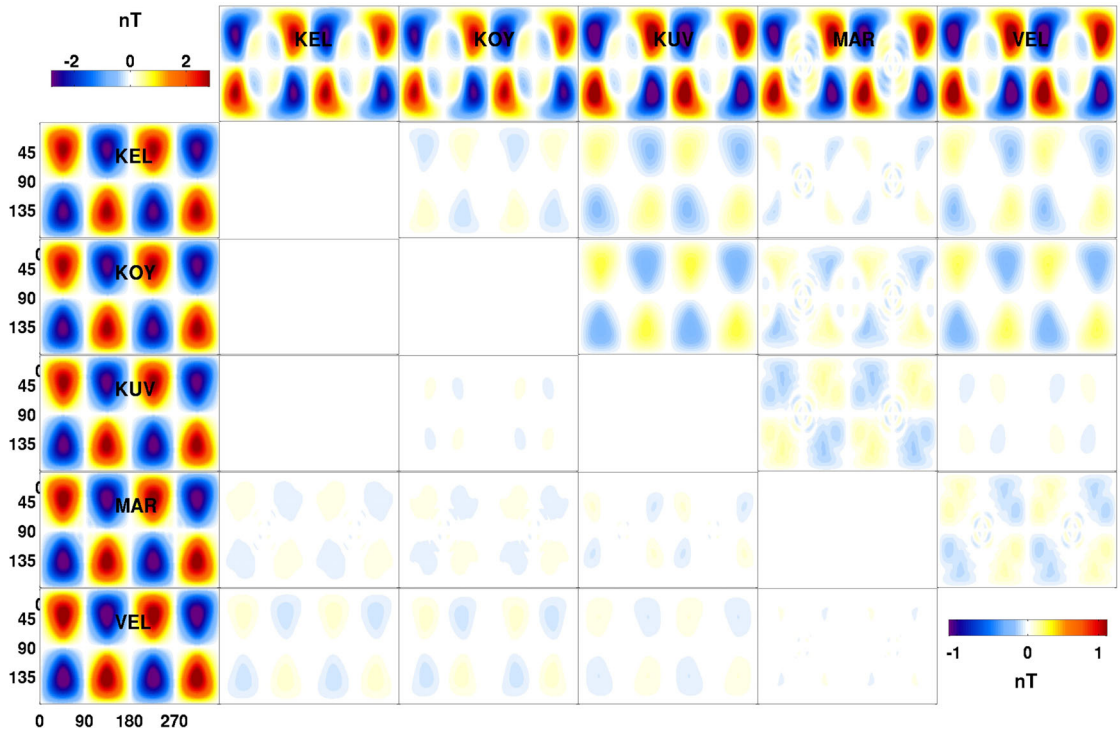

Figure 18. Real and imaginary parts of the ϕ-component of the magnetic field for benchmark case 5 $l = 2$ $m = 2$ at a single period (4 d). The first (vertical) column corresponds to the real part of the magnetic fields. The colourbar at the top corresponds to the real part. The first (horizontal) row is the imaginary part. The colourbar at the bottom corresponds to the imaginary part. The lower triangle are the differences between the real parts from different codes. The upper triangle are the differences between the imaginary parts from different codes. The diagonal is empty. The colour scales used for the differences have the same ranges as the corresponding real/imag parts but they are shifted to be centred around zero.

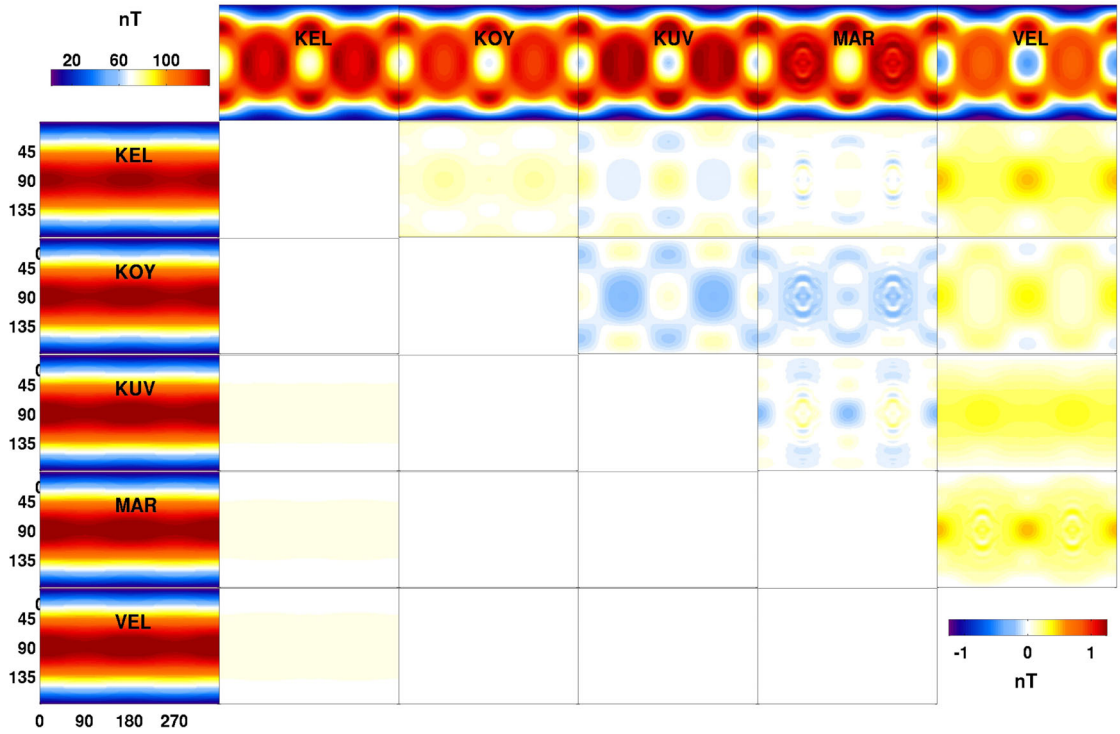

Figure 19. Real and imaginary parts of the θ-component of the magnetic field for benchmark case 5 $l = 2$ $m = 2$ at a single period (4 d). The first (vertical) column corresponds to the real part of the magnetic fields. The colourbar at the top corresponds to the real part. The first (horizontal) row is the imaginary part. The colourbar at the bottom corresponds to the imaginary part. The lower triangle are the differences between the real parts from different codes. The upper triangle are the differences between the imaginary parts from different codes. The diagonal is empty. The colour scales used for the differences have the same ranges as the corresponding real/imag parts but they are shifted to be centred around zero.

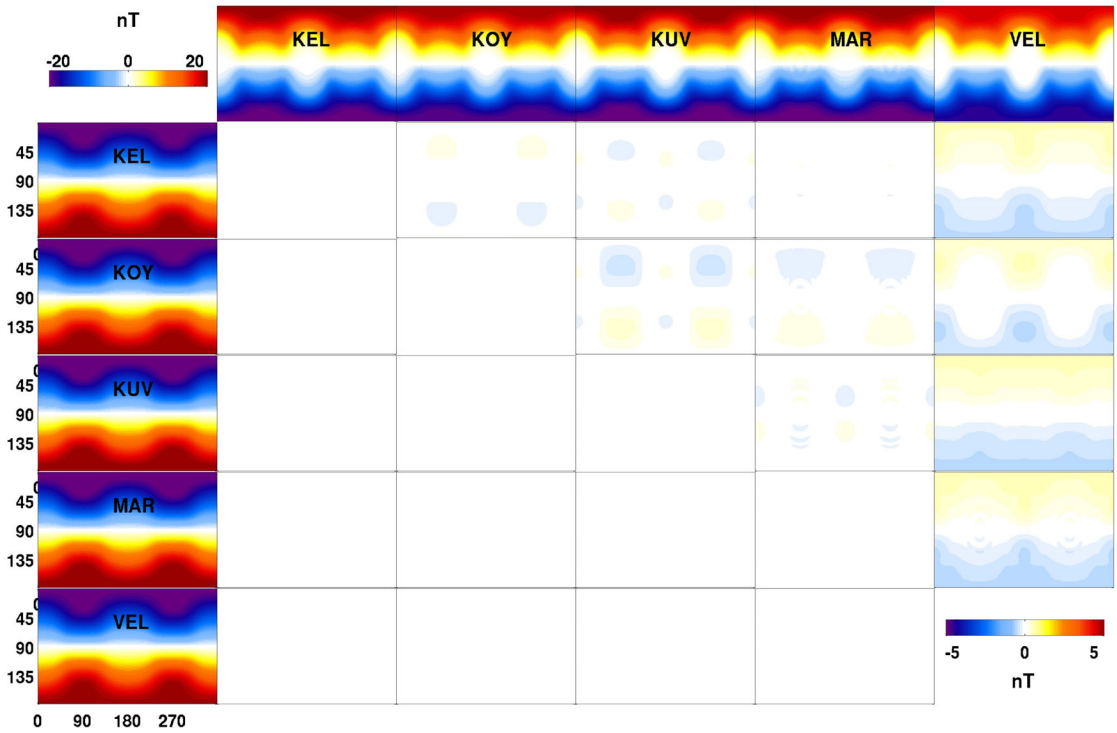

Figure 20. Real and imaginary parts of the radial component of the magnetic field for benchmark case 5 $l = 2$ $m = 2$ at a single period (4 d). The first (vertical) column corresponds to the real part of the magnetic fields. The colourbar at the top corresponds to the real part. The first (horizontal) row is the imaginary part. The colourbar at the bottom corresponds to the imaginary part. The lower triangle are the differences between the real parts from different codes. The upper triangle are the differences between the imaginary parts from different codes. The diagonal is empty. The colour scales used for the differences have the same ranges as the corresponding real/imag parts but they are shifted to be centred around zero.

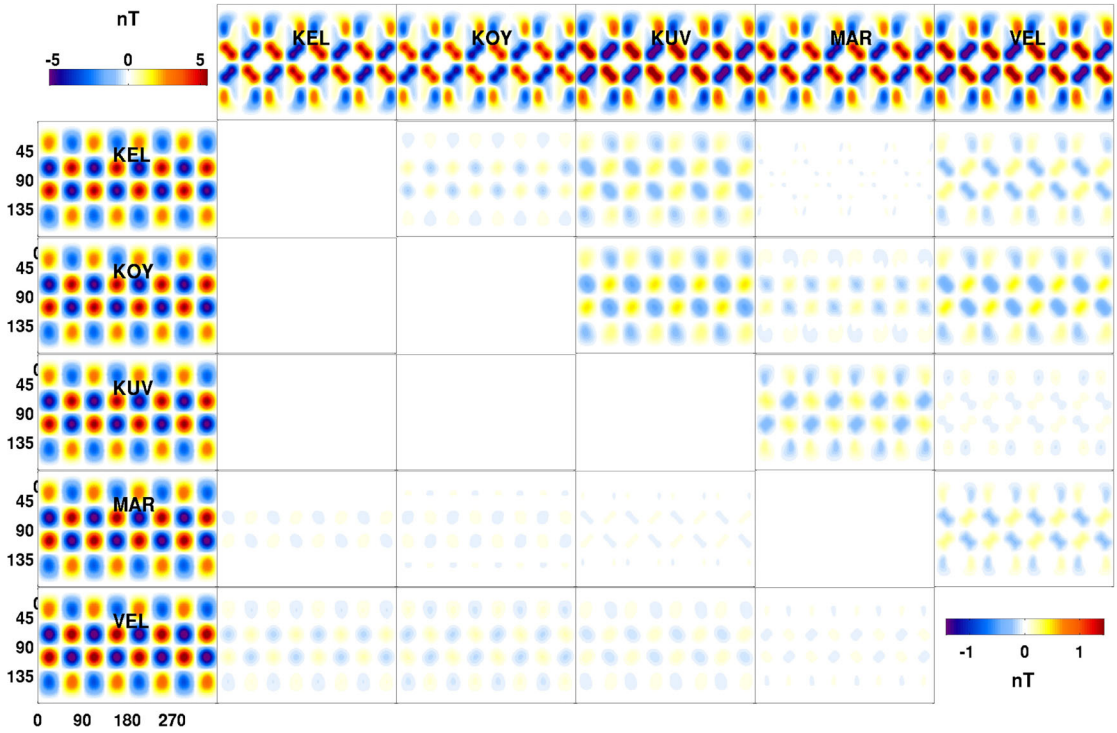

Figure 21. Real and imaginary parts of the ϕ-component of the magnetic field for benchmark case 5 $l = 6$ $m = 4$ at a single period (4 d). The first (vertical) column corresponds to the real part of the magnetic fields. The colourbar at the top corresponds to the real part. The first (horizontal) row is the imaginary part. The colourbar at the bottom corresponds to the imaginary part. The lower triangle are the differences between the real parts from different codes. The upper triangle are the differences between the imaginary parts from different codes. The diagonal is empty. The colour scales used for the differences have the same ranges as the corresponding real/imag parts but they are shifted to be centred around zero.

Figure 22. Real and imaginary parts of the θ-component of the magnetic field for benchmark case 5 $l = 6$ $m = 4$ at a single period (4 d). The first (vertical) column corresponds to the real part of the magnetic fields. The colourbar at the top corresponds to the real part. The first (horizontal) row is the imaginary part. The colourbar at the bottom corresponds to the imaginary part. The lower triangle are the differences between the real parts from different codes. The upper triangle are the differences between the imaginary parts from different codes. The diagonal is empty. The colour scales used for the differences have the same ranges as the corresponding real/imag parts but they are shifted to be centred around zero.

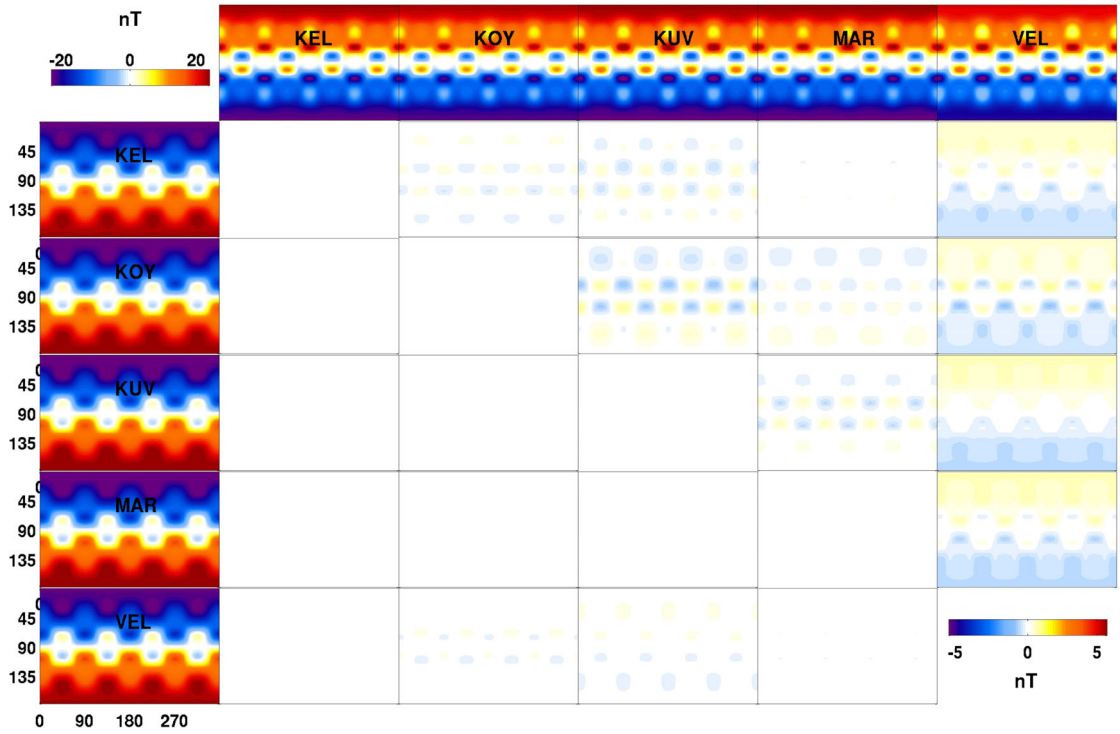

Figure 23. Real and imaginary parts of the radial component of the magnetic field for benchmark case 5 $l = 6$ $m = 4$ at a single period (4 d). The first (vertical) column corresponds to the real part of the magnetic fields. The colourbar at the top corresponds to the real part. The first (horizontal) row is the imaginary part. The colourbar at the bottom corresponds to the imaginary part. The lower triangle are the differences between the real parts from different codes. The upper triangle are the differences between the imaginary parts from different codes. The diagonal is empty. The colour scales used for the differences have the same ranges as the corresponding real/imag parts but they are shifted to be centred around zero.

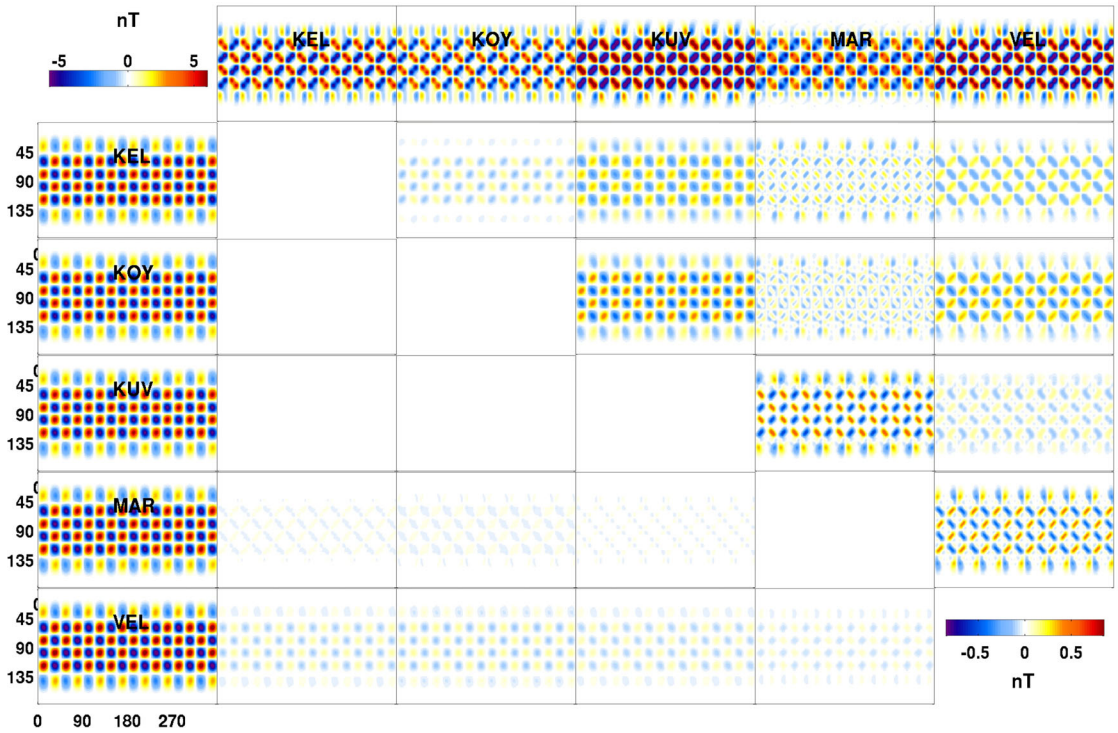

Figure 24. Real and imaginary parts of the ϕ-component of the magnetic field for benchmark case 5 $l = 12$ $m = 8$ at a single period (4 d). The first (vertical) column corresponds to the real part of the magnetic fields. The colourbar at the top corresponds to the real part. The first (horizontal) row is the imaginary part. The colourbar at the bottom corresponds to the imaginary part. The lower triangle are the differences between the real parts from different codes. The upper triangle are the differences between the imaginary parts from different codes. The diagonal is empty. The colour scales used for the differences have the same ranges as the corresponding real/imag parts but they are shifted to be centred around zero.

Figure 25. Real and imaginary parts of the θ-component of the magnetic field for benchmark case 5 $l = 12$ $m = 8$ at a single period (4 d). The first (vertical) column corresponds to the real part of the magnetic fields. The colourbar at the top corresponds to the real part. The first (horizontal) row is the imaginary part. The colourbar at the bottom corresponds to the imaginary part. The lower triangle are the differences between the real parts from different codes. The upper triangle are the differences between the imaginary parts from different codes. The diagonal is empty. The colour scales used for the differences have the same ranges as the corresponding real/imag parts but they are shifted to be centred around zero.

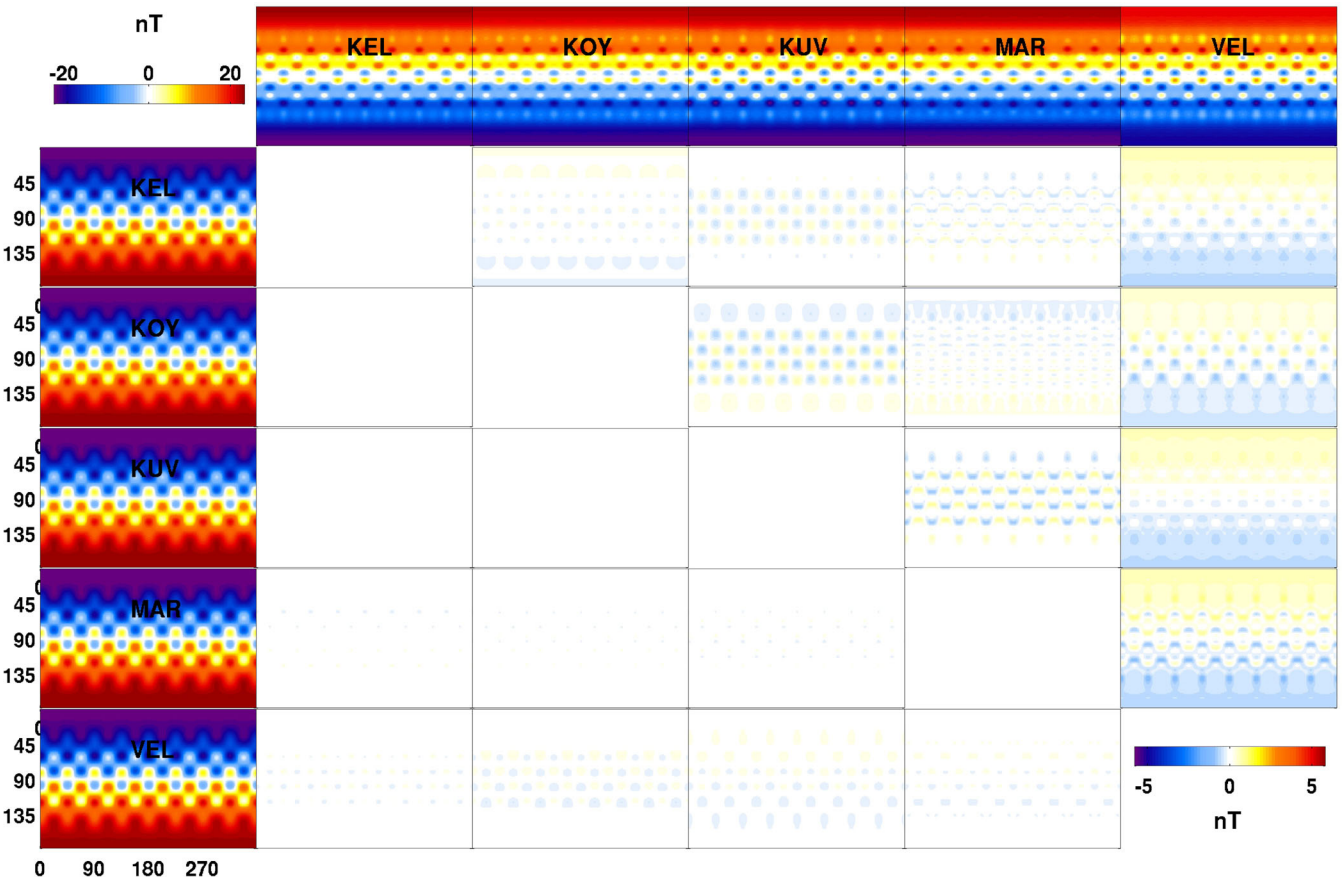

Figure 26. Real and imaginary parts of the radial component of the magnetic field for benchmark case 5 $l = 12$ $m = 8$ at a single period (4 d). The first (vertical) column corresponds to the real part of the magnetic fields. The colourbar at the top corresponds to the real part. The first (horizontal) row is the imaginary part. The colourbar at the bottom corresponds to the imaginary part. The lower triangle are the differences between the real parts from different codes. The upper triangle are the differences between the imaginary parts from different codes. The diagonal is empty. The colour scales used for the differences have the same ranges as the corresponding real/imag parts but they are shifted to be centred around zero.

Table 5. Radial background conductivity model used as a base for model 6.

Depths (km)	Conductivities (S m^{-1})
0–400	0.01
400–650	0.1
650–2871	2.0
2871–6371	500 000

again mostly focused around continent edges. These errors seem to have a latitudinal dependence.

In conclusion of our discussion, we also present these same results rotated back to geographic coordinates. These are illustrated in Figs 30–32. We can see that upon rotation, the effect of the P_1^0 source is dominant in the real parts of the tangential field components. However, the relative errors in the solutions are not significantly affected by rotation.

9 TECHNICAL DETAILS FOR ALL SOLUTIONS

Table 6 summarizes the contribution of each solution to different models.

It is worth noting that for all synthetic special cases presented in this study, the methods based on integral equation formulation (IE; KUV, KOY, and SUN) require significantly shorter CPU times than those of the full-Earth FE scheme (FE; RIB), full-Earth finite difference scheme (FD; KEL) and of the SHFE methods (SHFE; MAR, VEL). The CPU times of the FD method are comparable to those of SHFE schemes at similar accuracy levels (here, they are higher due to enhanced FD accuracy and resolution presented in this paper). On the other hand, the IE methods tend to require significantly more resources as the heterogeneous model domain is expanded to include all of Earth's mantle, while the computational requirements of the FD scheme are determined based on the numerical grid and will never exceed those presented in this paper even for a fully heterogeneous Earth. A major advantage of SHFE is a very modest memory requirement compared to the other methods.

By design of this study, all authors, independently, chose to stop their codes at the tolerance that they found appropriate to produce a sufficiently accurate solution. Since higher tolerance typically corresponds to higher accuracy and longer run times, this setting needs to be taken into account when model solutions and run times are compared. For this reason, we include information about the tolerance settings, where relevant, into the technical detail Tables 7–13.

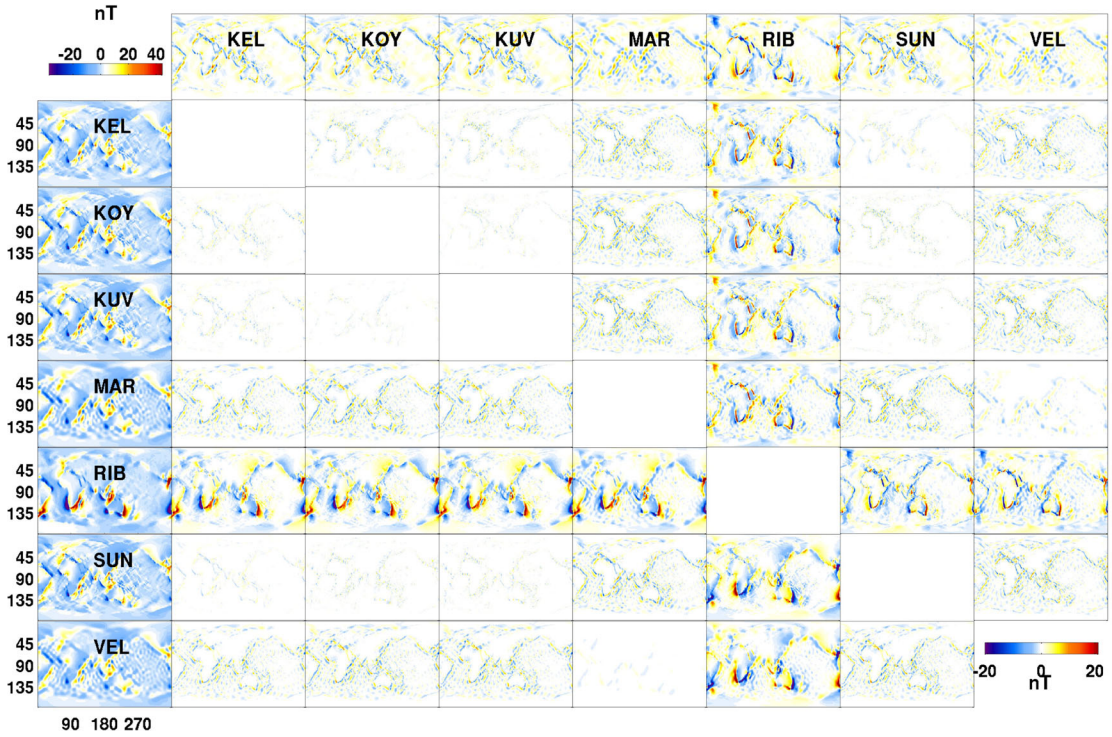

Figure 27. Real and imaginary parts of the ϕ-component of the magnetic field for benchmark case 6 at a single period (6 hr) in geomagnetic coordinates. The first (vertical) column corresponds to the real part of the magnetic fields. The colourbar at the top corresponds to the real part. The first (horizontal) row is the imaginary part. The colourbar at the bottom corresponds to the imaginary part. The lower triangle are the differences between the real parts from different codes. The upper triangle are the differences between the imaginary parts from different codes. The diagonal is empty. The colour scales used for the differences have the same ranges as the corresponding real/imag parts but they are shifted to be centred around zero.

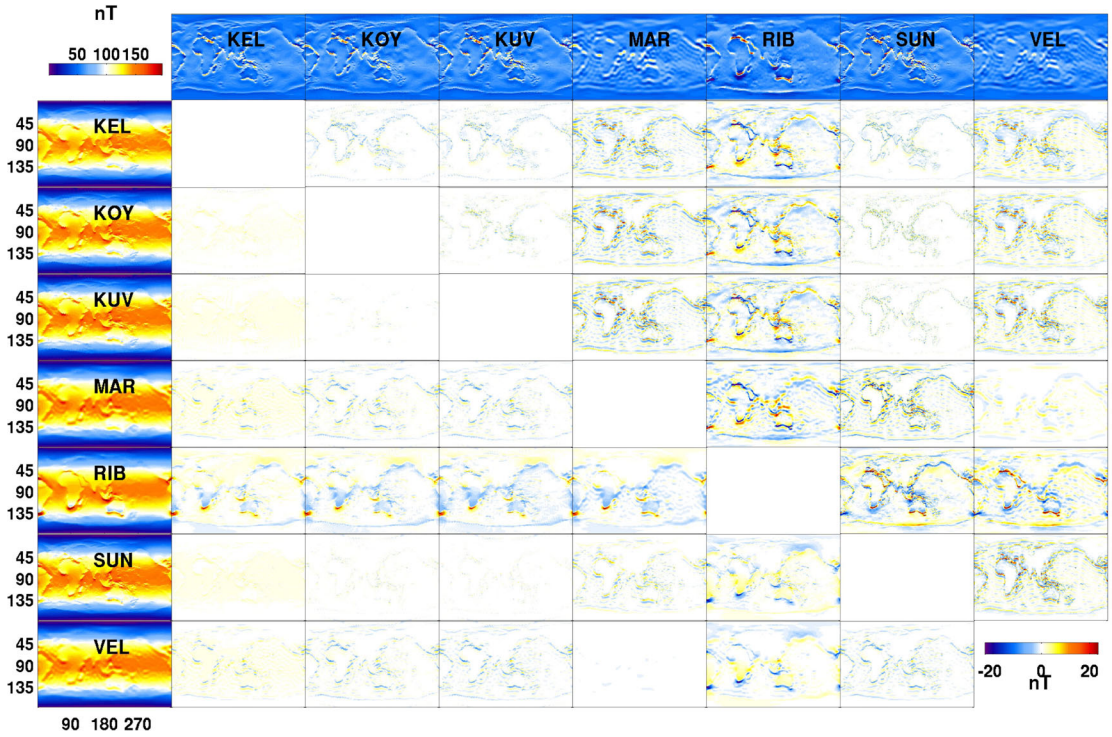

Figure 28. Real and imaginary parts of the θ-component of the magnetic field for benchmark case 6 at a single period (6 hr) in geomagnetic coordinates. The first (vertical) column corresponds to the real part of the magnetic fields. The colourbar at the top corresponds to the real part. The first (horizontal) row is the imaginary part. The colourbar at the bottom corresponds to the imaginary part. The lower triangle are the differences between the real parts from different codes. The upper triangle are the differences between the imaginary parts from different codes. The diagonal is empty. The colour scales used for the differences have the same ranges as the corresponding real/imag parts but they are shifted to be centred around zero.

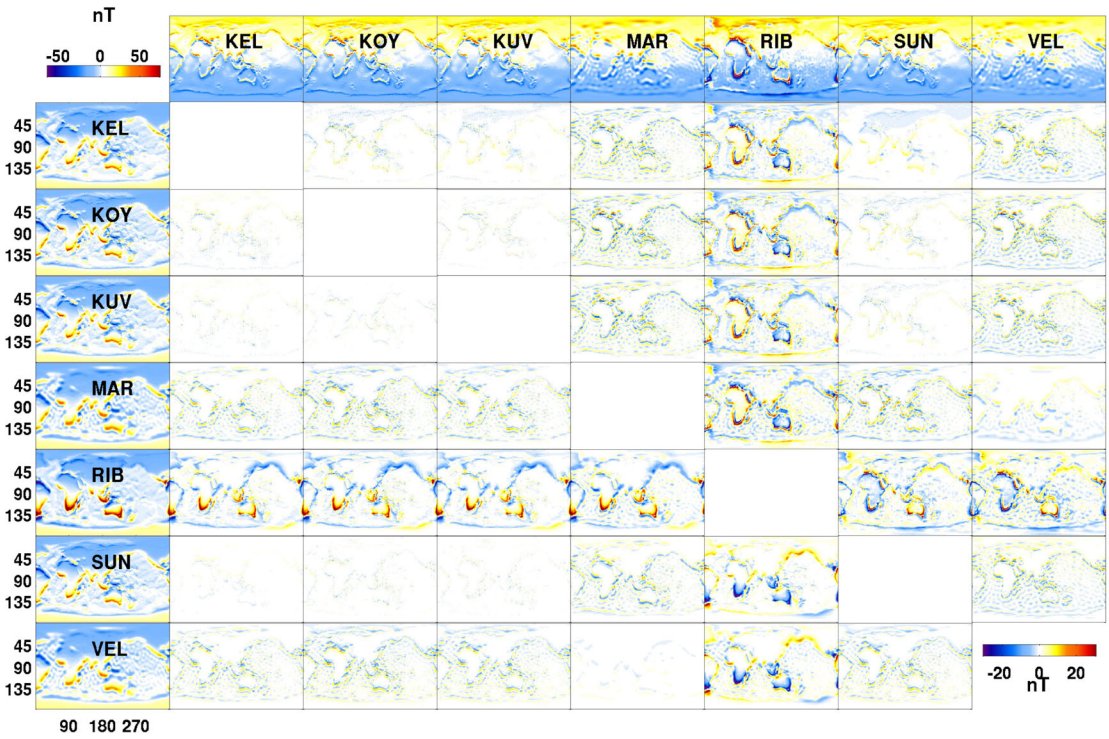

Figure 29. Real and imaginary parts of the radial component of the magnetic field for benchmark case 6 at a single period (6 hr) in geomagnetic coordinates. The first (vertical) column corresponds to the real part of the magnetic fields. The colourbar at the top corresponds to the real part. The first (horizontal) row is the imaginary part. The colourbar at the bottom corresponds to the imaginary part. The lower triangle are the differences between the real parts from different codes. The upper triangle are the differences between the imaginary parts from different codes. The diagonal is empty. The colour scales used for the differences have the same ranges as the corresponding real/imag parts but they are shifted to be centred around zero.

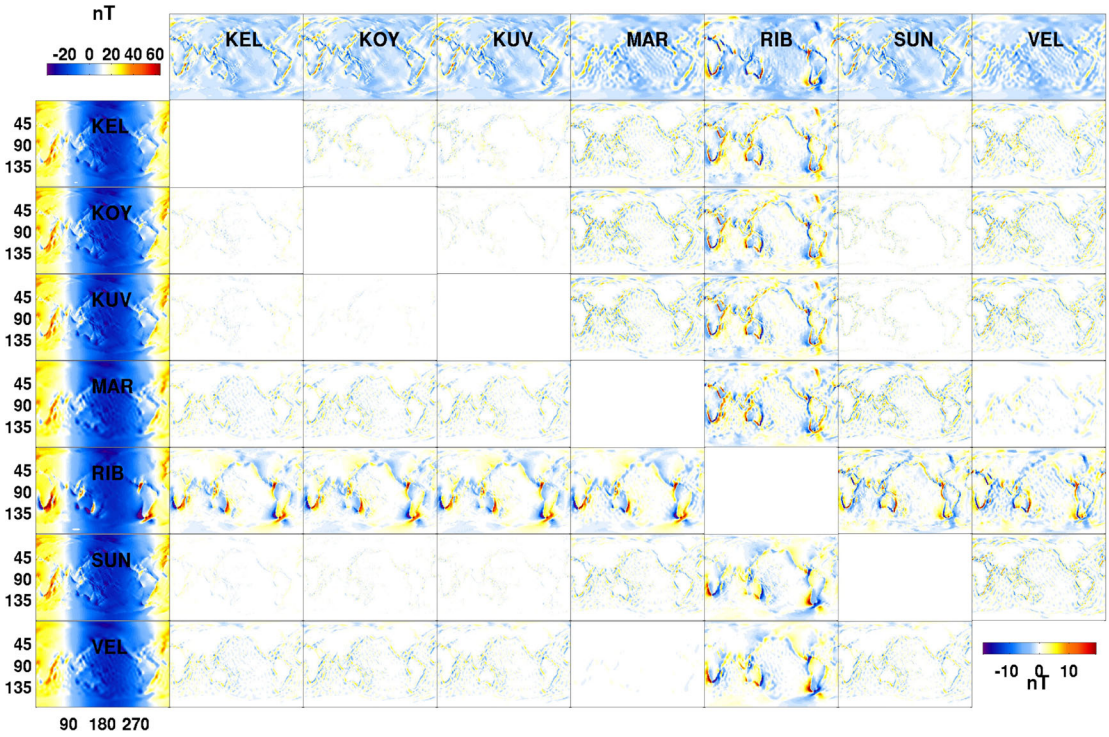

Figure 30. Real and imaginary parts of the ϕ-component of the magnetic field for benchmark case 6 at a single period (6 hr) in geographic coordinates. The first (vertical) column corresponds to the real part of the magnetic fields. The colourbar at the top corresponds to the real part. The first (horizontal) row is the imaginary part. The colourbar at the bottom corresponds to the imaginary part. The lower triangle are the differences between the real parts from different codes. The upper triangle are the differences between the imaginary parts from different codes. The diagonal is empty. The colour scales used for the differences have the same ranges as the corresponding real/imag parts but they are shifted to be centred around zero.

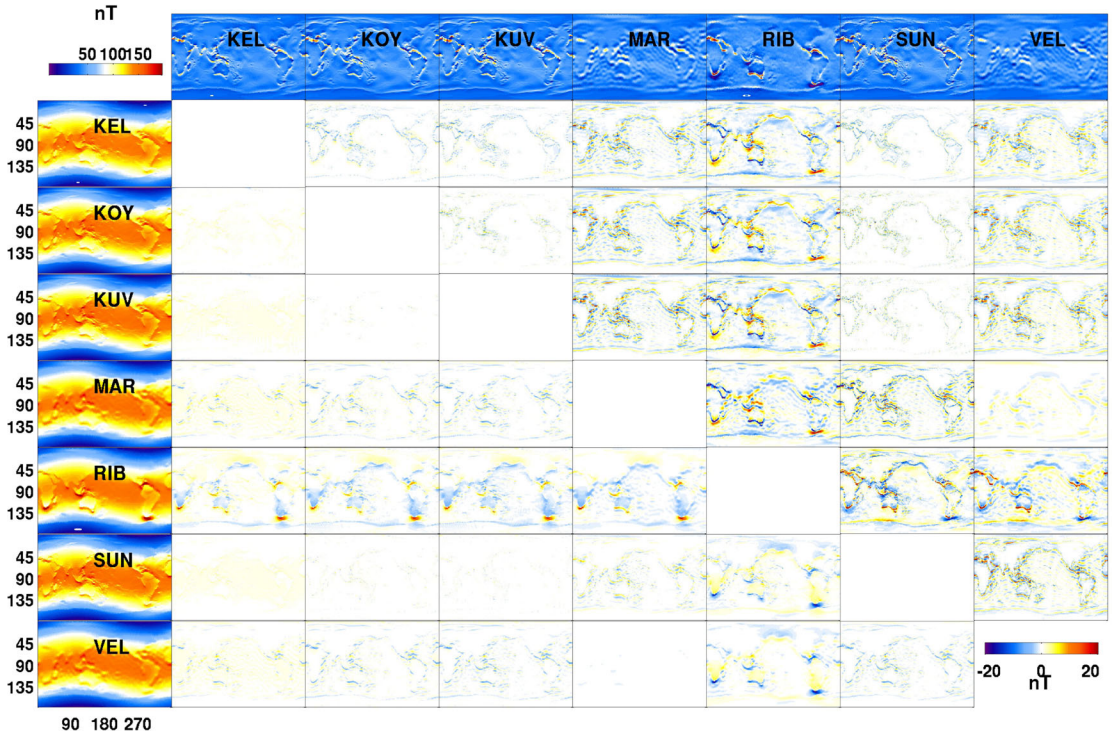

Figure 31. Real and imaginary parts of the θ-component of the magnetic field for benchmark case 6 at a single period (6 hr) in geographic coordinates. The first (vertical) column corresponds to the real part of the magnetic fields. The colourbar at the top corresponds to the real part. The first (horizontal) row is the imaginary part. The colourbar at the bottom corresponds to the imaginary part. The lower triangle are the differences between the real parts from different codes. The upper triangle are the differences between the imaginary parts from different codes. The diagonal is empty. The colour scales used for the differences have the same ranges as the corresponding real/imag parts but they are shifted to be centred around zero.

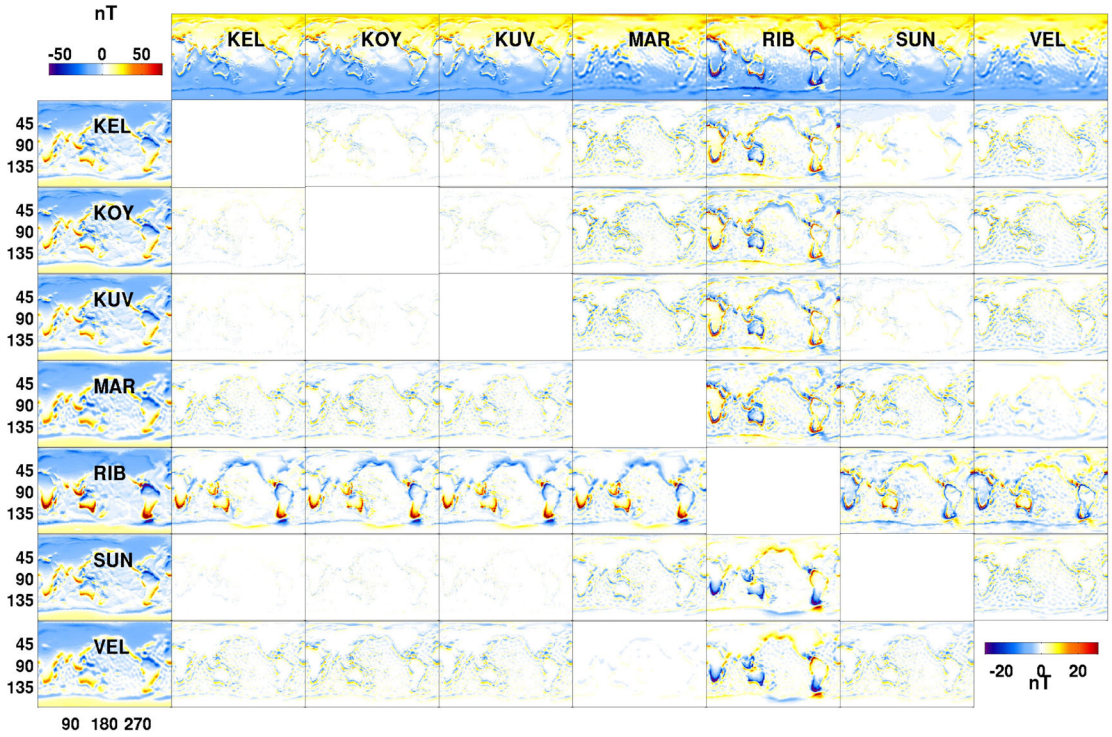

Figure 32. Real and imaginary parts of the radial component of the magnetic field for benchmark case 6 at a single period (6 hr) in geographic coordinates. The first (vertical) column corresponds to the real part of the magnetic fields. The colourbar at the top corresponds to the real part. The first (horizontal) row is the imaginary part. The colourbar at the bottom corresponds to the imaginary part. The lower triangle are the differences between the real parts from different codes. The upper triangle are the differences between the imaginary parts from different codes. The diagonal is empty. The colour scales used for the differences have the same ranges as the corresponding real/imag parts but they are shifted to be centred around zero.

Table 6. Contributions of individual codes to the benchmark.

Abbrev.	References	Model 1	Model 2	Model 3	Model 4	Model 5	Model 6
KEL	Uyeshima & Schultz (2000); Kelbert *et al*. (2008)	Yes	Yes	Yes	Yes	Yes	Yes
KOY	Koyama *et al*. (2006)	Yes	Yes	Yes	Yes	Yes	Yes
KUV	Kuvshinov (2008)	Yes	Yes	Yes	Yes	Yes	Yes
MAR	Martinec (1999)	Yes	Yes	Yes	Yes	Yes	Yes
RIB	Ribaudo *et al*. (2012)	Yes	Yes	Yes	—	—	Yes
SUN	Sun & Egbert (2012)	Yes	Yes	—	—	—	Yes
VEL	Velímský & Martinec (2005)	Yes	Yes	Yes	Yes	Yes	Yes

Table 7. Summary of technical details for finite difference solution by Uyeshima & Schultz (2000) (as modified by Kelbert *et al*. 2008) for different models. Numerical grid (in the form of $N_\phi \times N_\theta \times N_r$) stands for a number of volume cells used to obtain the solution. This number includes 17 air layers of the computational grid, and 8 layers representing the 'thinsheet'. CPU time is the maximum over the four frequencies, given for a single 2.6 GHz AMD Opteron(TM) 6238 processor. However, in practice the code is run in parallel (parallelized by frequency with MPI). The Fortran 90 code is compiled by Portland Group 12.2 64-bit compiler with options '-O3 -fastsse -mp -tp=istanbul-64'. Note that the achieved solution tolerance is very different depending on whether or not the secondary field formulation (SFF) or the full 3-D forward computation (FWD) was performed. This is because the 1-D structure is not included in the iterative scheme for SFF. Here, we include both values, where appropriate. Nevertheless, the accuracies of the resultant solutions are so similar, that this paper only presents one or the other—typically, SFF, if computed; run times are also similar between these two methods. The convergence criterion (used to control the iterative scheme) is less strongly dependent on the method we employ. The number of iterations stated in this table is the number of calls to divergence correction, averaged between the four frequencies. For Model 5, all values are representative for this class of models, averaged between the three model configurations.

Model	Numerical grid	CPU time	Tolerance (SFF/FWD)	Convergence criterion (SFF/FWD)	N of div. corr.	Memory requirements (Mb)
Model 1	$360 \times 180 \times 98$	7 hr	$10^{-3}/10^{-29}$	$10^{-6}/10^{-7}$	45	8516
Model 2	$360 \times 180 \times 98$	6 hr	$10^{-3}/10^{-27}$	$10^{-6}/10^{-7}$	32	8516
Model 3	$360 \times 180 \times 119$	7 hr	$-/10^{-30}$	$-/10^{-8}$	25	9290
Model 4	$360 \times 180 \times 119$	6.5 hr	$-/10^{-30}$	$-/10^{-8}$	21	9290
Model 5	$360 \times 180 \times 98$	1.5 hr	$10^{-3}/-$	$10^{-6}/-$	10	8516
Model 6	$360 \times 180 \times 98$	7.5 hr	$10^{-4}/-$	$10^{-7}/-$	23	8516

Table 8. Summary of technical details for CIE solution by Kuvshinov (2008) for different models. Numerical grid (in a form of $N_\phi \times N_\theta \times N_r$) stands for a number of volume cells used to obtain the solution. CPU time is for a single frequency for a single core processor on dual-core 2.8 GHz AMD Opteron 2220 processor. The code is written in Fortran 77 and compiled by Intel 13.0 compiler with no optimization flags. The resulting system of equations $Ax = b$ is solved by Krylov subspace iterations. Tolerance defines the threshold to stop the iterations; in other words it is assumed that the approximation to the solution, $x^{(n)}$, is obtained once the following inequality holds: $||Ax^{(n)} - b||/||b|| < \epsilon$.

Model	Numerical grid	Overall CPU time	CPU time (CIE)	CPU time (Green's fn)	Tolerance	No. of iterations	Memory requirements (Mb)
Model 1	$360 \times 180 \times 1$	2 min 2 s	9 s	1 min 47 s	10^{-4}	11	355
Model 2	$360 \times 180 \times 1$	2 min 2 s	9 s	1 min 47 s	10^{-4}	11	355
Model 3	$180 \times 90 \times 12$	56 min	9 min	43 min	10^{-4}	17	14 400
Model 4	$360 \times 180 \times 4$	45 min	6 min	37 min	10^{-4}	9	6400
Model 5	$360 \times 180 \times 2$	13 min	10 s	11 min	10^{-4}	11	1600
Model 6	$360 \times 180 \times 1$	2 min 2 s	9 s	1 min 47 s	10^{-4}	11	355

Table 9. Summary of technical details for CIE solution by Koyama *et al*. (2006) for different models. Numerical grid (in a form of $N_\phi \times N_\theta \times N_r$) stands for a number of volume cells used to obtain the solution. SPH degree is a truncation degree of spherical harmonic expansion. The code is written in Fortran 77 and compiled by gfortran compiler with no optimization flags. CPU time is for a single processor core on the laptop PC with a 2.6GHz Dual-Core Intel Core i5 processor in the 6 hr period case.

Model	Numerical grid	SPH degree	Overall CPU time	CPU time (CIE)	CPU time (Green's fn)	Tolerance	No. of iterations	Memory requirements (Mb)
Model 1	$360 \times 180 \times 1$	230	6 min	4.5 min	1.5 min	10^{-7}	26	2300
Model 2	$360 \times 180 \times 1$	230	9 min	7.5 min	1.5 min	10^{-7}	48	2300
Model 3	$360 \times 180 \times 24$	135	68 min	67 min	1 min	10^{-7}	31	3240
Model 4	$360 \times 180 \times 20$	120	65 min	64 min	1 min	10^{-7}	40	2740
Model 5	$360 \times 180 \times 5$	100	7 min	6.5 min	0.5 min	10^{-7}	19	1320
Model 6	$360 \times 180 \times 1$	150	2 min	1.5 min	0.5 min	10^{-7}	13	1420

9.1 Finite difference solution (KEL)

At the core of the code, which is written in Fortran 90, is the efficient finite difference forward solver written by Uyeshima & Schultz (2000). While the code has been in general heavily modified for inversion by Kelbert *et al*. (2008), the forward solver is functionally identical to the Uyeshima & Schultz (2000) original code, modified by Toh *et al*. (2002). The system $Ax = b$ is solved with a stabilized version of the biconjugate gradient method [BiCGStab; Toh *et al*. (2002)], with periodic 'divergence

Table 10. Summary of technical details for CIE solution by Sun & Egbert (2012) for different models. Numerical grid (in a form of $N_\phi \times N_\theta \times N_r$) stands for numbers of surface cells used to obtain the solution. The system matrix equation $Ax = b$ is solved with Krylov subspace iterations. The Krylov iteration stops when $||A\hat{x} - b||/||b|| < \epsilon$, where $\hat{x}$ is the approximate solution, and ϵ is the stopping tolerance. The code is written in MATLAB. The CPU time is measured under MATLAB R2012a for a single processor core on an Apple iMac desktop with a 2.8 GHz Quad-Core Intel Core i5 processor.

Model	Numerical grid	Overall CPU time	CPU time (CIE)	CPU time (Green's fn)	Tolerance	No. of iterations	Memory requirements (Mb)
Model 1	$360 \times 180 \times 1$	30 min	10 s	30 min	10^{-6}	25	358
Model 2	$360 \times 180 \times 1$	30 min	10 s	30 min	10^{-6}	25	358
Model 6	$360 \times 180 \times 1$	30 min	11 s	30 min	10^{-6}	25	358

Table 11. Summary of technical details for SHFE-FD solution by Martinec (1999) for different models. Spatial resolution is given by spherical harmonic truncation degree $j_{\max}$, and number of layers $k_{\max}$. CPU time is reported for a single 2.0 GHz x86-64 processor. The Fortran 77 code was compiled by Intel Fortran Compiler v 13.0.1 with default optimization. The number of iterations was fixed, and the resulting tolerance (relative error of the right-hand side of the linear system) was always 10^{-4} or less.

Model	$j_{\max}$	$k_{\max}$	CPU time	N of iterations	Memory requirements (Mb)
Model 1	40	132	2 hr	101	940
Model 2	40	132	2 hr	101	940
Model 3	40	151	2.5 hr	101	1230
Model 4	40	96	1.5 hr	101	500
Model 5	40	123	2 hr	101	820
Model 6	40	148	2.5 hr	101	1190

Table 12. Summary of technical details for SHFE-TD solution by Velímský & Martinec (2005) for different models. Spatial resolution is given by spherical harmonic truncation degree $j_{\max}$, and number of layers $k_{\max}$. The time-step Δt is selected according to the period T. CPU time is reported for a single 2.0 GHz x86-64 processor, and post-processing (in particular, Fourier transform of the results) is excluded. The Fortran 90 code was compiled by Intel Fortran Compiler v 13.0.1 with default optimization, and using Intel Math Kernel Library v 11.0 for LAPACK subroutines.

Model	$j_{\max}$	$k_{\max}$	Δt	No. of time steps	CPU time	Memory requirements (Mb)
Model 1	40	132	$T/6000$	60 000	1.7 hr	140
Model 2	40	132	$T/6000$	60 000	1.7 hr	140
Model 3	40	151	$T/6000$	60 000	2.3 hr	180
Model 4	40	96	$T/6000$	60 000	1.2 hr	75
Model 5	40	123	$T/6000$	60 000	1.7 hr	120
Model 6	40	148	$T/6000$	60 000	2.3 hr	170

Table 13. Summary of technical details for FE solution by Ribaudo *et al.* (2012) for different models. Number of nodes and cells reflects cumulative adaptive refinements for all four frequencies. Reported runtime is wall clocktime, not charged CPU time, for all frequencies run sequentially, including mesh generation and refinement. Tolerance refers to maximum allowed relative error in each cell for potentials, not fields. It is defined by the program setting 'errlim', which is set at 0.003 for this study. This means that, in every cell of the mesh, each variable has an error less than 0.3 per cent of the value of that variable within the cell. Errors higher than this will trigger adaptive refinement of the mesh. All models are run with four simultaneous CPU threads, using the default parallelization of FlexPDE 6.19 package on a MacPro running Windows Vista with two 2.80 GHz x64 quad-core processors.

Model	Nodes	Cells	Runtime	Tolerance	Memory requirements (MB)
Model 1	473 058	348 181	3.8 hr	10^{-3}	4 108 812
Model 2	726 394	534 065	142 hr	10^{-3}	25 810 521
Model 3	124 207	91 698	17.9 hr	10^{-3}	3 262 615
Model 6	471 328	344 337	169 hr	10^{-3}	18 054 692

corrections' [see Uyeshima & Schultz (2000)]. The divergence correction procedure is called at least once every 60 BiCGStab iterations. The stopping criterion requires that one of the two conditions of either 1) the convergence criterion $\sqrt{||x^{(n)} - x^{(n-1)}||/||x^{(n)}||} < \delta$, or 2) tolerance $||Ax^{(n)} - b||/||b|| < \epsilon$ are achieved. In practice, $\epsilon =$ 1e-30 to protect against numerical saturation, and the convergence criterion δ is used to tighten or relax the accuracy of the solution, as shown in Table 7.

Finite difference methods do not have an inherent preference for smooth models over sharp model contrasts, or vice versa, however the numerical solution converges faster for smooth models. Accurate representation of complicated geometries with a structured

finite difference grid requires high resolution and cranks up the computational requirements. For a regular latitude/longitude grid, accuracy increases as we get away from the poles, where convergence is worst.

Any remaining artifacts (e.g. see Fig. 2b at the North pole) may be eliminated completely if the solution is allowed to converge further. They are amplified if the convergence criteria are relaxed. We are not certain that this is an inherent feature of staggered-grid finite difference approach, since the South pole—which is also a singularity—does not seem to exhibit this behaviour. Whether a feature or a bug, this issue does not seem to affect mid-latitude results. Instead, the solutions at the mid-latitudes (and specifically at the conductive/resistive interfaces) are essentially unaffected by the convergence criteria, if these are varied within a reasonable range.

9.2 Integral equation solutions (KUV, KOY, and SUN)

Table 8 lists the gridding, convergence and computational loads of IE code by Kuvshinov (2008) for different models.

Table 9 lists the gridding, convergence and computational loads of integral equation solution by Koyama *et al*. (2006) for different models. SPH degree is the truncation degree of spherical harmonic expansions to be used in the code for the mode expansions (details in Koyama *et al*. 2013). The maximum degree of the spherical harmonics as well as the spherical Bessel functions depends on the arguments to be calculated numerically, that is, the background conductivity structure and the frequency. Thus the SPH degree differs in each model.

Table 10 lists the gridding, convergence and computational loads of integral equation solution by Sun & Egbert (2012) for different models.

Methods based on integral equation with a contracting kernel allow for an efficient and accurate simulation of EM fields both in smooth models, and models with sharp contrasts. The convergence to the solution is very fast irrespectively of the conductivity contrasts, and run times are from small to moderate. The solvers based on this approach work equally well for models with simple and complicated geometries.

9.3 SHFE solutions (MAR, VEL)

Tables 11–12 list the respective gridding, convergence and computational loads of the frequency-domain and time-domain SHFE solutions by Martinec (1999) and Velímský & Martinec (2005) for different models.

SHFE methods are good at representing smooth model variations with a handful of basis functions, but dealing with sharp contrasts (such as the ocean/continent interfaces) is problematic. We have experimented with various techniques to suppress the ringing artifacts in the scenarios with sharp conductivity contrasts. These included linear and cosine tapering of conductivities across the interfaces, or a least-squares projections of the (logarithm of) conductivity into the space spanned by spherical harmonics. However, while ringing was ameliorated, these changes lead to increased systematic shifts of the solutions compared to other techniques. Therefore, we decided to leave the ringing untreated in all presented results.

The semi-analytical solution for the nested-sphere model 3 presented in Section 5 was obtained at truncation degree $j_{\max} = 24$.

9.4 Finite element solution (RIB)

Table 13 lists the gridding, convergence and computational loads of the FE solution by Ribaudo *et al*. (2012) for different models. Each model is staged in order of decreasing period, because higher frequencies usually require finer mesh. The FE mesh is adaptively refined for each frequency and then passed on for use in the following stage. The numbers in the table reflect the cumulative totals from all four frequencies.

FE methods provide an unprecedented degree of geometric flexibility, including grid adaptation, and are therefore good at representing complicated structures and sharp contrasts; however, convergence is slow for complicated geometries and requires large run times for accuracy.

10 CONCLUSIONS

We have presented a careful benchmark exercise for a very heterogeneous set of seven global electromagnetic induction modelling codes, including three CIE formulations, two SHFE solutions, a regular staggered-grid FD method and an adaptive grid FE solution. We have employed a set of synthetic examples of varying complexity to assess their performance and relative consistency.

The three codes based on CIE concept are shown to be highly efficient for all synthetic examples, and compare well between themselves as well as to the other solvers in all regions of the globe including poles. The two key components of any CIE formulation are the computation of the Green's tensor and the numerical solution of CIE, respectively. In the code of Koyama *et al*. (2006, KOY), the main computational load goes to the numerical solution of CIE, whereas in the codes by Kuvshinov (2008, KUV) and Sun & Egbert (2012, SUN) the Green's tensor computation is the most time-consuming part of the codes. This feature puts the latter two codes at a computational advantage when repeated numerical solutions are required, such as for solving source and/or conductivity inverse problems. Indeed, as long as the background model remains unchanged, Green's tensors only need to be computed once, and may be reused for multiple sources, as well as for varying electrical conductivity distributions.

In contrast to FD and FE formulations that solve sparse matrix systems, the CIE codes work with dense matrices (with all entries filled), but these matrices are much more compact than matrices used in FD and FE codes. The reason for compactness is that in the CIE codes the modelling region is confined only to the spherical layers that contain the inhomogeneities, whereas in the FD and FE codes one has to discretize a much larger volume in the radial direction in order to enable the decay (or stabilization) of the fields at the upper and lower boundaries of the domain. Also note that the CIE matrices do not require preconditioning irrespective of discretization, frequency and contrasts of conductivity. Because of this, for local geometries, FD code by Kelbert *et al*. (2008, KEL) and FE code by Ribaudo *et al*. (2012, RIB) are much more computationally demanding than CIE formulations. This is no longer true when the computational domain is expanded to include a fully heterogeneous Earth's mantle. The computational requirements of CIE surge rapidly with the expanded size of the model domain, resulting in run times more comparable to Kelbert *et al*. (2008, KEL) and in very demanding memory requirements for Green's tensor computation and storage in Kuvshinov (2008, KUV). Note that the 3-D CIE code of Koyama *et al*. (2006, KOY) is not as demanding in terms of memory requirements.

FD code by Kelbert *et al*. (2008, KEL) based on Uyeshima & Schultz (2000) is equally efficient with local and globally distributed contrasts, but requires high grid resolution to resolve sharp contrasts and complicated geometries. At the resolution and accuracy levels considered in this manuscript, the FD results compare well to those of the other solvers and do not exhibit any noticeable artifacts. At lower accuracy levels, convergence is poorest at the poles, however the solutions at the model contrasts are not affected, and computational requirements drop significantly.

The FE solution of Ribaudo *et al*. (2012, RIB) tends to introduce significant errors where structures are present, and noise away from the heterogeneities. It is also one of the most computationally demanding approaches out of those considered in this paper. While adaptive grid FE approach provides an unprecedented degree of geometric flexibility, the use of general-purpose modelling software presents its challenges. Even though the modelling algorithm can be guided by user-adjustable settings, the ability to optimize the algorithm for solving the induction equation in particular is not available, resulting in longer run times than would be necessary with purpose-built code. In particular, the run times for the computations presented in the paper have been insufficient to provide adequately accurate solutions.

SHFE methods Martinec (1999, MAR) and Velímský & Martinec (2005, VEL) tend to be most accurate away from sharp contrasts, which also introduce global ringing effects in SHFE solutions, but are otherwise equally efficient with all model types. Like CIE codes and Ribaudo *et al*. (2012, RIB), they do not suffer from discretization problems at the poles. They are tailored to scenarios where both the source field and the observed induced field are parametrized globally by spherical harmonic functions. Such base is a natural choice for processing of satellite observations recorded along low-altitude polar orbits. On the other hand, interpretation of coastal observatory data by global SHFE modelling could be biased by significant modelling errors. The single-frequency periodic regime is not a typical scenario for the deployment of the time-domain method, as its run times scale linearly with the length of the time series. Nevertheless, it provides results comparable to the frequency-domain method using the same spatial discretization.

Our analysis has provided an overview of the magnitude of numerical errors in these global electromagnetic modelling codes that are otherwise very difficult to constrain. These findings should be taken into account when these codes are used in practice.

Overall, we conclude that even though these methods are all very different in their numerical approaches and implementation, all modelling results are reasonably consistent with each other, suggesting that (with reservations discussed above) these solutions are all equally valid in approaching the problem of global electromagnetic induction, and may be employed for practical global geomagnetic inversion.

ACKNOWLEDGEMENTS

Kelbert acknowledges the support of NASA grant NNX08AG04G. Kelbert also thanks the authors of the original forward solver Makoto Uyeshima and Adam Schultz for giving her access to their code, and Jin Sun for access to his 1-D forward modelling code in Matlab which helped develop and test the secondary field formulation. Kuvshinov acknowledges the support of Russian Foundation for Basic Research under grant No. 13-05-12111. Ribaudo acknowledges the support of Scripps Institution of Oceanography, and NASA Headquarters under the NASA Earth and Space Science Fellowship Program – Grant NNX07AQ94H. Velimsky acknowledges the support of the Grant Agency of Czech Republic, Project No. P210/11/1366.

REFERENCES

Avdeev, D.B. & Knizhnik, S., 2009. 3D integral equation modeling with a linear dependence on dimensions, *Geophysics,* **74,** 89–94.

Avdeev, D.B., Kuvshinov, A., Pankratov, O. & Newman, G., 2000. 3-D EM modelling using fast integral equation approach with Krylov subspaces accelerator, in *Proceedings of the 2nd EAGE Conference and Technical Exhibition,* Vol. 2, 2nd EAGE Conference and Technical Exhibition, Scotland.

Avdeev, D.B., Kuvshinov, A., Pankratov, O. & Newman, G.A., 2002. Three-dimensional induction logging problems, Part I: an integral equation solution and model comparisons, *Geophysics,* **67**(2), 413–426.

Christensen, U. *et al.*, 2001. A numerical dynamo benchmark, *Phys. Earth planet. Inter.,* **128**(14), 25–34.

Egbert, G.D. & Kelbert, A., 2012. Computational recipes for electromagnetic inverse problems, *Geophys. J. Int.,* **189,** 251–167.

Everett, M.E. & Schultz, A., 1995. Geomagnetic induction in eccentrically nested spheres, *Phys. Earth planet. Inter.,* **92**(3-4), 189–198.

Everett, M.E. & Schultz, A., 1996. Geomagnetic induction in a heterogenous sphere: azimuthally symmetric test computations and the response of an undulating 660-km discontinuity, *J. geophys. Res. (Solid Earth),* **101**(B2), 2765–2783.

Everett, M.E., Constable, S.C. & Constable, C.G., 2003. Effects of near-surface conductance on global satellite induction responses, *Geophys. J. Int.,* **153**(1), 277–286.

Fainberg, E., Kuvshinov, A. & Singer, B., 1990. Electromagnetic induction in a spherical Earth with non-uniform oceans and continents in electric contact with the underlying medium, I. Theory, method and example, *Geophys. J. Int.,* **102,** 273–281.

Fainberg, E.B. & Zinger, B., 1980. Electromagnetic induction in a nonuniform spherical model of the Earth, *Ann. Geophys.,* **36,** 127–134.

Fujii, I. & Schultz, A., 2002. The 3D electromagnetic response of the earth to ring current and auroral oval excitation, *Geophys. J. Int.,* **151**(3), 689–709.

Hamano, Y., 2002. A new time-domain approach for the electromagnetic induction problem in a three-dimensional heterogeneous earth, *Geophys. J. Int.,* **150,** 753–769.

Hursan, G. & Zhdanov, M., 2002. Contraction integral equation method in three-dimensional electromagnetic modeling, *Radio Science,* **37,** doi:10.1029/2001RS002513.

Karato, S.-I., 1990. The role of hydrogen in the electrical conductivity of the upper mantle, *Nature,* **347,** 272–273.

Karato, S.-I., 2011. Water distribution across the mantle transition zone and its implications for global material circulation, *Earth planet. Sci. Lett.,* **301**(3-4), 413–423.

Kelbert, A., Egbert, G.D. & Schultz, A., 2008. Non-linear conjugate gradient inversion for global EM induction: resolution studies, *Geophys. J. Int.,* **173**(2), 365–381.

Kelbert, A., Schultz, A. & Egbert, G.D., 2009. Global electromagnetic induction constraints on transition-zone water content variations, *Nature,* **460**(7258), 1003–1006.

Koyama, T., Shimizu, H. & Utada, H., 2002. Possible effects of lateral heterogeneity in the D″ layer on electromagnetic variations of core origin, *Phys. Earth planet. Inter.,* **129,** 99–116.

Koyama, T., Shimizu, H., Utada, H., Ichiki, M., Ohtani, E. & Hae, R., 2006. Water content in the mantle transition zone beneath the North Pacific derived from the electrical conductivity anomaly, *AGU Geophys Monogr Ser.,* **168,** 171–179.

Koyama, T., Utada, H. & Avdeev, D.B., 2008. Fast and memory-saved 3-D forward modeling code for MT by using integral equation method, in *Abstract Book, Proceedings of the 19th Workshop on Electromagnetic induction in the Earth,* China.

Koyama, T., Khan, A. & Kuvshinov, A., 2013. Three-dimensional electrical conductivity structure beneath Australia from inversion of geomagnetic

observatory data: evidence for lateral variations in transition-zone temperature, water content and melt, *Geophys. J. Int.,* doi: 10.1093/gji/ggt455.

Kuvshinov, A., 2008. 3-D Global induction in the oceans and solid earth: recent progress in modeling magnetic and electric fields from sources of magnetospheric, ionospheric and oceanic origin, *Surv. Geophys.,* **29**(2), 139–186.

Kuvshinov, A. & Semenov, A., 2012. Global 3-D imaging of mantle electrical conductivity based on inversion of observatory C-responses–I. An approach and its verification, *Geophys. J. Int.,* **189**(3), 1335–1352.

Kuvshinov, A., Avdeev, D.B. & Pankratov, O., 1999. Global induction by Sq and Dst sources in the presence of oceans: bimodal solutions for non-uniform spherical surface shells above radially symmetric Earth models in comparison to observations, *Geophys. J. Int.,* **137**(3), 630–650.

Kuvshinov, A., Avdeev, D.B., Pankratov, O., Golyshev, S.A. & Olsen, N., 2002. Modelling electromagnetic fields in 3D spherical Earth using fast integral equation approach, in *3D Electromagnetics,* Chapter 3, pp. 43–54, eds Zhdanov, M.S. & Wannamaker, P.E., Elsevier.

Kuvshinov, A., Utada, H., Avdeev, D.B. & Koyama, T., 2005. 3-D modelling and analysis of Dst C-responses in the North Pacific Ocean region, revisited, *Geophys. J. Int.,* **160**(2), 505–526.

Mackie, R.L., Smith, J.T. & Madden, T.R., 1994. 3-Dimensional electromagnetic modeling using finite-difference equations—the magnetotelluric example, *Radio Sci.,* **29**(4), 923–935.

Martinec, Z., 1989. Program to calculate the spectral harmonic expansion coefficients of the two scalar fields product, *Comput. Phys. Commun.,* **54**(1), 177–182.

Martinec, Z., 1998. Geomagnetic induction in multiple eccentrically nested spheres, *Geophys. J. Int.,* **132,** 96–110.

Martinec, Z., 1999. Spectral-finite element approach to three-dimensional electromagnetic induction in a spherical Earth, *Geophys. J. Int.,* **136,** 229–250.

Medin, A.E., Parker, R.L. & Constable, S.C., 2007. Making sound inferences from geomagnetic sounding, *Phys. Earth planet. Inter.,* **160**(1), 51–59.

Miensopust, M.P., Queralt, P. & Jones, A.G. the 3D MT modellers, 2013. Magnetotelluric 3-d inversion—a review of two successful workshops on forward and inversion code testing and comparison, *Geophys. J. Int.,* **193**(3), 1216–1238.

Pankratov, O., Avdeev, D.B. & Kuvshinov, A., 1995. Electromagnetic field scattering in a homogeneous Earth: a solution to the forward problem, *Phys. Solid. Earth,* **31,** 201–209.

Pankratov, O., Kuvshinov, A. & Avdeev, D.B., 1997. High-performance three-dimensional electromagnetic modeling using modified Neumann series. Anisotropic case, *J. Geomag. Geoelectr.,* **49,** 1541–1547.

Qin, Y., Capdeville, Y., Maupin, V., Montagner, J.-P., Lebedev, S. & Beucler, E., 2008. Spice benchmark for global tomographic methods, *Geophys. J. Int.,* **175**(2), 598–616.

Ribaudo, J.T., Constable, C.G. & Parker, R.L., 2012. Scripted finite element tools for global electromagnetic induction studies, *Geophys. J. Int.,* **188,** 435–446.

Semenov, A. & Kuvshinov, A., 2012. Global 3-D imaging of mantle conductivity based on inversion of observatory C -responses-II. Data analysis and results, *Geophys. J. Int.,* doi: 10.1111/j.1365-246X.2012.05665.x.

Singer, B.S., 1995. Method for solution of Maxwell's equations in non-uniform media, *Geophys. J. Int.,* **120**(3), 590–598.

Singer, B.S., 2008. Electromagnetic integral equation approach based on contraction operator and solution optimization in Krylov subspace, *Geophys. J. Int.,* **175**(3), 857–884.

Singer, B.S. & Fainberg, E.B., 1995. Generalization of the iterative dissipative method for modeling electromagnetic fields in nonuniform media with displacement currents, *J. appl. Geophys.,* **34,** 41–46.

Singer, B.S. & Fainberg, E.B., 1997. Fast and stable method for 3D modeling of electromagnetic field, *Explor. Geophys.,* **34,** 130–135.

Spada, G. *et al.*, 2011. A benchmark study for glacial isostatic adjustment codes, *Geophys. J. Int.,* **185**(1), 106–132.

Sun, J. & Egbert, G.D., 2012. A thin-sheet model for global electromagnetic induction, *Geophys. J. Int.,* **189**(1), 343–356.

Tarits, P. & Mandéa, M., 2010. The heterogeneous electrical conductivity structure of the lower mantle, *Phys. Earth planet. Inter.,* **183**(1-2), 115–125.

Toh, H., Schultz, A., Uyeshima, M. & Fujii, I., 2002. Three-dimensional modelling of the Earth's mantle—Biconjugate gradient solution, in *Proceedings of the Ocean Hemisphere Project 2,* Tokyo.

Uyeshima, M. & Schultz, A., 2000. Geomagnetic induction in a heterogeneous sphere: a new three-dimensional forward solver using a conservative staggered-grid finite difference method, *Geophys. J. Int.,* **140**(3), 636–650.

Velímský, J. & Martinec, Z., 2005. Time-domain, spherical harmonic-finite element approach to transient three-dimensional geomagnetic induction in a spherical heterogeneous Earth, *Geophys. J. Int.,* **160**(1), 81–101.

Weiss, C.J., 2010. Triangulated finite difference methods for global-scale electromagnetic induction simulations of whole mantle electrical heterogeneity, *Geochem. Geophys. Geosyst.,* **11**(11), 1525–2027.

Yoshimura, R. & Oshiman, N., 2002. Edge-based finite element approach to the simulation of geolectromagnetic induction in a 3-D sphere, *Geophys. Res. Lett.,* **29**(3), 91–94.

Yoshino, T., Matsuzaki, T., Shatskiy, A. & Katsura, T., 2009. The effect of water on the electrical conductivity of olivine aggregates and its implications for the electrical structure of the upper mantle, *Earth planet. Sci. Lett.,* **288**(1-2), 291–300.

Zhong, S., McNamara, A., Tan, E., Moresi, L. & Gurnis, M., 2008. A benchmark study on mantle convection in a 3-D spherical shell using citcoms, *Geochem., Geophys., Geosyst.,* **9**(10), doi:10.1029/2008GC002048.